

A Radar-Based Hail Climatology of Australia

JORDAN P. BROOK^{a,b} JOSHUA S. SODERHOLM,^b ALAIN PROTAT,^b HAMISH MCGOWAN,^a AND ROBERT A. WARREN^b

^a Atmospheric Observations Research Group, University of Queensland, Queensland, Australia

^b Science and Innovation Group, Australian Bureau of Meteorology, Docklands, Victoria, Australia

(Manuscript received 22 June 2023, in final form 17 November 2023, accepted 2 January 2024)

ABSTRACT: In Australia, hailstorms present considerable public safety and economic risks, where they are considered the most damaging natural hazard in terms of annual insured losses. Despite these impacts, the current climatological distribution of hailfall across the continent is still comparatively poorly understood. This study aims to supplement previous national hail climatologies, such as those based on environmental proxies or satellite radiometer data, with more direct radar-based hail observations. The heterogeneous and incomplete nature of the Australian radar network complicates this task and prompts the introduction of some novel methodological elements. We introduce an empirical correction technique to account for hail reflectivity biases at C band, derived by comparing overlapping C- and S-band observations. Furthermore, we demonstrate how object-based hail swath analysis may be used to produce resolution-invariant hail frequencies, and describe an interpolation method used to create a spatially continuous hail climatology. The maximum estimated size of hail (MESH) parameter is then applied to a mixture of over 50 operational radars in the Australian radar archive, resulting in the first nationwide, radar-based hail climatology. The spatiotemporal distribution of hailstorms is examined, including their physical characteristics, seasonal and diurnal frequency, and regional variations of such properties across the continent.

KEYWORDS: Atmosphere; Australia; Climatology; Hail; Radars/Radar observations; Remote sensing

1. Introduction

Hailstorms account for a substantial portion of financial impacts caused by natural hazards globally, resulting in greater than 10 billion USD in insured losses annually in the United States alone (Gunturi and Tippett 2017). In Australia, hail is typically considered the costliest natural hazard in terms of insured losses, exceeding the combined losses of both bushfires and floods (Schuster et al. 2006; McAneney et al. 2019). Several of the country's most populous cities have experienced hailstorms that resulted in over 1 billion AUD in losses, including Melbourne in the south (Buckley et al. 2010; Allen 2012), Perth on the west coast (Buckley et al. 2010), and most frequently Brisbane and Sydney on the east coast (Soderholm et al. 2019; Schuster et al. 2006). Financial losses also appear to be increasing alongside an expansion of the built environment (Changnon et al. 2009), and as of 2019 in Australia, 7 of the 10 most damaging events occurred in the past decade (adjusted for inflation, Eichner 2019). The significance of these financial impacts underscores the need to quantify the current level of hail hazard in the region.

Numerous studies have investigated the climatology of hailstorms in Australia using various data sources, including hail reports, hail proxies from weather models, and remote sensing observations from satellite radiometers and weather radars. First, studies based on the Bureau of Meteorology's Severe Storms Archive are limited by well-documented reporting biases for hail observations (Allen and Tippett 2015). Population biases are particularly prominent in Australia, which has the fifth lowest population density globally. These problems are compounded by

the fact that 87% of the already limited population resides within 50 km of the coast, leaving vast areas (mostly in the country's arid interior) effectively unobserved (Australian Bureau of Statistics 2021). Consequently, climatological studies based on hail reports are restricted to more populated regions such as eastern New South Wales (Schuster et al. 2005). Changes in reporting practices further diminish the practical value of this dataset (Walsh et al. 2016), especially for more recent years where the archive has been poorly maintained. The most comprehensive analysis of hail reports in Australia is provided by Allen and Allen (2016), offering valuable verification for the results that follow.

Perhaps the most common approach for estimating the climatological distribution of hail on regional scales involves identifying "hail-prone" environmental conditions from numerical weather prediction (NWP) models. In these studies, an environment is considered "hail-prone" based on a combination of favorable model indices, such as convective available potential energy (CAPE) or 0–6-km bulk vertical wind shear (see Raupach et al. 2023, and references therein). Such an approach is appealing from a climatological standpoint due to the spatiotemporal continuity of the underlying model data, and has formed the basis of several global (e.g., Prein and Holland 2018) and Australian (e.g., Allen and Karoly 2014) hail and severe storm climatologies. While these studies have contributed valuable insights into the distribution of hail events worldwide, they must be interpreted with some caution. First, the exact formation of the "optimal" hail proxy varies considerably between studies and different climatic regions (Zhou et al. 2021), often resulting in an overestimation of the tropical hail frequency in Australia (Bednarczyk and Soudounis 2012; Allen and Karoly 2014; Prein and Holland 2018). Recent research by Raupach et al. (2023) addresses these concerns in an Australian context by training their proxy on

Corresponding author: Jordan Brook, j.brook@uq.edu.au

Australian hail reports, and allowing their formulation to vary latitudinally, which more accurately characterized hail environments across the country. However, the accuracy of this approach is limited by the representativeness of the underlying hail report dataset, which is affected by the aforementioned biases involving population density and reporting practices. Moreover, hail proxies are known to suffer from the “initiation problem,” whereby only a small fraction of hail-prone environments (often less than 10%, Taszarek et al. 2020) actually undergo convective initiation (Tippett et al. 2015). This issue ultimately leads to large uncertainties regarding the true climatological frequency of hailfall. In an Australian context, this problem spuriously highlights a spatial hail frequency maximum over the ocean on the east coast (e.g., Prein and Holland 2018). These oceanic overestimations likely stem from an absence of known convection trigger mechanisms for the region, such as sea-breeze or topographic interactions (Soderholm et al. 2017b). Raupach et al. (2023) demonstrated that incorporating a series of additional environmental constraints could successfully reduce the false alarm rate for Australian hailstorms, improving the critical success index (CSI) to ~ 0.3 when compared to hail reports.

Recent climatological studies also attempt to address the initiation problem by confirming convective initiation through passive spaceborne observations of deep convection. While passive infrared imagers aboard geostationary satellites cannot detect hail directly (Murillo and Homeyer 2019), some studies have used these observations to identify dynamical characteristics associated with hailstorms, such as above anvil cirrus plumes (Levizzani and Setvák 1996; Homeyer et al. 2017) or overshooting tops (OT; Schmetz et al. 1997; Bedka et al. 2010). OT detections have been combined with hail proxies to produce regional hail climatologies in numerous studies (e.g., Bedka et al. 2018; Punge et al. 2021), and although this methodology likely improves on those derived from hail proxies alone, significant uncertainty still remains when associating OT detections with hail at the surface. Bedka et al. (2018) found that only 28% of OT detections are spatiotemporally associated with hail reports in Australia (within 1 h and 50 km), which is also considerably lower than 50% in Europe (Bedka 2011) and the United States (Dworak et al. 2012). Despite these uncertainties, the Bedka et al. (2018) hail climatology of Australia is a significant advancement in our understanding of hail in remote areas of the continent, and serves as a valuable reference for this study.

One final class of satellite-based hail climatologies relevant for our investigation involves hail detections from passive microwave radiometers and precipitation (Ku/Ka band) radars aboard low-Earth orbit satellites. Studies have shown that simple brightness temperature (BT) thresholds at certain frequencies correctly subset hail-bearing storms in the United States with 40% accuracy (Cecil 2009; Ferraro et al. 2015). This principle has been employed to generate several global hail climatologies (e.g., Cecil 2009; Cecil and Blankenship 2012; Ferraro et al. 2015). Subsequent research with spaceborne precipitation radars by Ni et al. (2017) revealed that similar to hail proxies, these passive microwave methods overestimate the amount of hail in tropical regions such as northern Australia due to regional variations in thunderstorm structure. These insights have been used to more accurately

detect hail events ($CSI \approx 0.28$ relative to ground-radar-based hail detections, Mroz et al. 2017), and updated global hail climatologies based on these improvements will also serve as important secondary validation for our study (Mroz et al. 2017; Ni et al. 2017; Bang and Cecil 2019).

Indirect hail detection methods from hail proxies, geostationary satellites, or passive microwave radiometers each have distinct limitations, which ultimately contributes to uncertainty in their resulting climatologies. In light of these constraints, weather radars offer an appealing alternative for climatological hail studies. These instruments provide spatiotemporally uniform, three-dimensional, direct measurements of hydrometeors, making them ideal for climatological studies, assuming sufficient archive length and spatial coverage (Saltikoff et al. 2019). When restricted to single-polarized radar data (as is the case in Australia), the maximum estimate size of hail (MESH; Witt et al. 1998) parameter emerges as perhaps the most thoroughly validated hail diagnostic. Although MESH is not a reliable predictor of hail sizes (Wilson et al. 2009; Ortega 2018), it has been shown to usefully discriminate hail occurrence within thunderstorms (Cintineo et al. 2012; Ortega 2018; Murillo and Homeyer 2019). MESH has also been used to generate numerous regional hail climatologies in Europe (e.g., Kunz and Kugel 2015; Lukach et al. 2017) and the United States (Cintineo et al. 2012; Wendt and Jirak 2021). The latter were created using the U.S. NEXRAD radar archive, which represents the “gold standard” for radar networks from a climatological standpoint, consisting of over 160 identical radars operating over three decades. In contrast, the Australian radar network is highly diverse in terms of archive length, beamwidth, frequency, and receiver type (Soderholm et al. 2022), and covers only $\sim 30\%$ of the country’s total land surface. To date, these factors have limited radar-based hail studies to simple diurnal/seasonal analyses in 10 locations (Dowdy et al. 2020), or more detailed regional climatologies for 18 years in Brisbane (Soderholm et al. 2017a) and 8 years in Brisbane and Sydney (Warren et al. 2020).

In this study, our objective is to expand on previous work by creating a national hail climatology. To achieve this goal, we detail how we must address the unique challenges posed by the Australian radar archive, including normalizing differences in radar frequency and archive durations, and interpolating between large regions with no observations. These methodological elements are outlined in section 2 (methodology) and section 3 (radar frequency correction). We begin our analysis at a continental scale in section 4, by generating Australia’s first national radar-based hail climatology. We then identify five regions of interest within the national climatology to investigate on a regional scale in section 5, providing a more comprehensive analysis for each. Finally, we summarize our findings and suggest directions for future work in section 6.

2. Methodology

a. Data processing

The radar data used in this study are obtained from Level 1b of the Operational Radar Dataset in the Australian Unified Radar Archive (AURA, Soderholm et al. 2022). Our

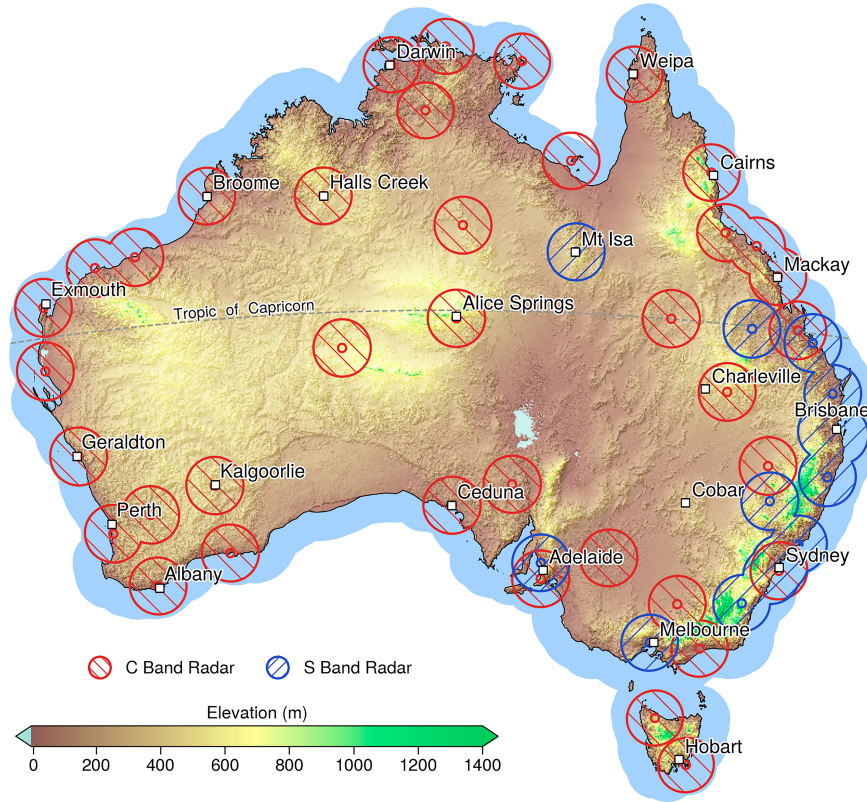


FIG. 1. An illustration of the radar network used in this study. Contours demonstrate the spatial data coverage of the radar network (ranges 20–140 km), with C- and S-band radars in red and blue, respectively. The ocean within 140 km of the mainland, excluding islands other than Tasmania, is filled with blue, and background shading illustrates topography.

analysis encompasses all available data between 2000 and 2022, and mandates that each radar must contain over five years of operational observations in order to be included. Certain radars have also been excluded due to data quality concerns, such as geographically remote radars that did not historically transmit volumetric data, radars with persistent beam blockages, and various airport radars that are unsuitable for meteorological applications. These restrictions narrow our analysis to 52 radars, as illustrated in Fig. 1. Among the 52 radars examined, only 8 are polarimetric¹ and 14 are S bands (wavelengths \sim 10 cm); both of which have important implications for our study, and merit separate discussions in sections 2b and 3, respectively. The Level 1b dataset contains quality controlled radar data in polar coordinates, and due to the single-polarization limitations for most of the archive, the horizontally polarized equivalent radar reflectivity factor (Z , hereafter reflectivity) is used exclusively for hail detection. A filtering procedure is applied to remove ground clutter contamination (Gabella and Notarpietro 2002; Heistermann et al. 2013), and radar reflectivity is calibrated

using a ground clutter monitoring and spaceborne radar comparison technique (refer to Louf and Protat 2023, for additional details). The latter is particularly important for our purposes, as calibration errors are known to severely impact hail size estimates (e.g., Warren et al. 2020). Recent three-way calibration checks for the Australian archive (between ground-based, ship-based, and spaceborne radars, Protat et al. 2022) have found that postcorrection calibration errors fall within ± 0.5 dB, theoretically leading to acceptable MESH errors of less than 5% (Warren et al. 2020, their appendix A).

Special consideration must be given for data quality issues when using radar data for climatological studies, particularly when the climatological variable in question may be strongly affected by weak nonmeteorological echoes, such as chaff, anomalous propagation and sidelobe contamination (e.g., Fabry et al. 2017). These effects are unlikely to impact our results, given the relative echo strength and the elevated nature of the observations used to derive MESH (>3-km altitude). A possible exception may arise when spurious high-altitude, high-reflectivity echoes are detected due to ground clutter from elevated topography, especially during atmospheric conditions conducive to anomalous propagation. We contend that these cases occur infrequently in the Australian network due to the absence of prominent topographic features (highest peaks \sim 1500 m, Fig. 1), and direct the reader to the geometric

¹ The Bureau of Meteorology's Radar and Observation Network Uplift program dictates that all newly installed radars are polarimetric. At the time of writing, 16 of the 66 current operational radars are polarimetric, with this number expected to rise in years to come.

justification given in section 3.5 of [Nisi et al. \(2018\)](#) for a highly mountainous region. As in previous studies (e.g., [Cintineo et al. 2012](#)), a manual quality control procedure was applied to all identified hailstorms in the archive, which eliminated 1342 individual hail detections deemed spurious by a trained observer. We have determined that these evidently erroneous radar returns (such as complete volume saturation of >100 -dBZ reflectivity) are likely attributable to hardware or signal processing failures and predominantly occur in the earlier portions of the archive for older radars.

The final data processing consideration involves the amalgamation of overlapping reflectivity observations from individual radars. Previous studies have highlighted the importance of integrating information from multiple radars in order to fill gaps in radar scanning strategies and compensate for range dependencies ([Stumpf et al. 2004](#); [Ortega et al. 2006](#)). However, recent research by [Brook et al. \(2022\)](#) showed that gridding methods used to merge data into mosaics can degrade data quality, primarily through oversmoothing in the case of weighted average methods (e.g., [Langston et al. 2007](#)). Nearest-neighbor and linear interpolation methods can also propagate observational noise and introduce first-order discontinuities into the analysis (e.g., [Lakshmanan et al. 2006](#)). Single-polarized hail detection methods are highly dependent on the vertical distribution of reflectivity columns, the reconstruction of which is considerably degraded by both of the aforementioned gridding artifacts. Consequently, we have opted to regrid reflectivity observations using the variational interpolation method outlined by [Brook et al. \(2022\)](#) for each radar separately in our study, with a grid spacing of 1 km horizontally and 500 m vertically. This approach allows for quality control of individual radars without removing or recalculating the resulting mosaic when erroneous data from one radar is removed and ensures that isolated radars with no overlapping coverage are processed in the same manner as those that overlap. However, it also requires an additional post-processing step to merge the resulting hail detections for overlapping radars, which is detailed in [section 2b](#). We deemed the regridding process essential in order to capitalize on its superior characterization of deep convective plumes, despite the considerable computational resources required for applying the variational approach to all hail events in the archive. These methodological improvements ensure that the gridded reflectivities are closest to those at the native resolution of the radar, where the original MESH constants were defined ([Witt et al. 1998](#)).

b. Hail identification

The MESH parameter ([Witt et al. 1998](#)) is used for hail detection in this study. Although originally developed as an object-based, single-valued parameter, we adopt the common approach of calculating MESH on regular grids (e.g., [Stumpf et al. 2004](#)). This process begins with the calculation of the kinetic energy flux based on the semiempirical relationship first introduced by [Waldvogel et al. \(1978\)](#):

$$\dot{E} = 5.0 \times 10^{-6} \times 10^{0.084Z}, \quad (1)$$

where Z is in logarithmic units (dBZ). The hail kinetic energy flux is subsequently integrated across height levels that are

cold enough ($<0^\circ\text{C}$) and possess reflectivities large enough (>40 dBZ) to likely result from hail. Formally, these constraints are implemented through piecewise linear weighting functions for both conditions [$W(T)$ and $W(Z)$, respectively]. The weighted, vertical integration of hail kinetic energy flux results in a parameter termed the severe hail index (SHI), which is formalized as follows:

$$\text{SHI} = \frac{1}{10} \int_{H_0}^{H_{\text{top}}} W(Z)W(T)\dot{E} dH, \quad (2)$$

where H_0 is the height of the 0°C isotherm and H_{top} is the echo-top height. Finally, [Witt et al. \(1998\)](#) established the MESH formulation by empirically fitting SHI values to the 75th percentile of 147 hail report sizes, yielding $\text{MESH} = 2.54(\text{SHI})^{0.5}$. [Murillo and Homeyer \(2019\)](#) recently refit the SHI–MESH relationship using more than 5000 hail reports; however, these updated constants are not used here due to the alternate radar processing methods used in that study.² MESH has proven to be an effective hail discriminator; however, the exact MESH threshold used to detect hail varies slightly in the literature. Threshold values were defined to optimally identify severe/damaging hail, and several relevant studies and their corresponding MESH thresholds are given in [Table 1](#). Given the similarity among these five preceding studies and the aforementioned $\sim 5\%$ MESH errors associated with radar calibration, we deem it appropriate to take the average across them, which, when rounded to the nearest millimeter, results in a threshold of 30 mm.

We address the discrete temporal sampling rate of weather radars by implementing an advection correction algorithm from the PySTEPS package ([Pulkkinen et al. 2019](#)). This method interpolates MESH values along storm tracks by shifting values at time t forward and values at time $t + 1$ backward, before linearly weighting the two fields according to their temporal proximity ([Anagnostou and Krajewski 1999](#)). Advection velocities are calculated across the domain by applying the Lucas–Kanade optical flow method to the MESH fields. The procedure is applied over contiguous time periods with valid hail detections (volumes with ≥ 30 -mm MESH), and temporal interpolation is performed at minute intervals. These time periods are calculated such that hail detections separated by less than or equal to 30 min are grouped together. This threshold was selected to accommodate earlier years of the archive that had 10-min (rather than 5 min) volume sampling times, ensuring hail streaks³ from a single storm are not artificially split in cases with missing volumes due to hardware or communication failures.

² [Murillo and Homeyer \(2019\)](#) used a multi-radar reflectivity mosaic, smoothed using weighted average interpolation (GridRad; [Homeyer and Bowman 2017](#)). MESH estimates are extremely sensitive to reflectivity biases ([Warren et al. 2020](#)), meaning the SHI–MESH relationship derived for smoothed reflectivities is not suitable for the high-resolution grids used here ([Brook et al. 2022](#)).

³ We follow the terminology outlined in [Changnon \(1970\)](#) by referring to a *hail streak* as “an area of continuous hail with temporal coherence, which is considered an entity of hail generated within a thunderstorm.” A combination of spatiotemporally proximal hail streaks may then be subjectively grouped to form a *hail swath* for an event.

TABLE 1. MESH thresholds used to identify severe/damaging hail in various studies. Refer to each study for further details on the MESH matching/thresholding procedure used therein.

Study	Hail metric	Threshold (mm)
Wilson et al. (2009)	Hail reports ≥ 19 mm	28
Cintineo et al. (2012)	Hail reports ≥ 19 mm	29
Ortega (2018)	Hail reports ≥ 25.4 mm	30
Murillo and Homeyer (2019)	Hail reports ≥ 25.4 mm	29
Warren et al. (2020)	Insured hail damage	32

Our analysis then departs from conventional MESH studies by adopting an object-oriented approach, where individual hail streaks are created by contouring interpolated MESH grids at the 30-mm level. Each hail streak is defined by the 30-mm contour polygon, and an example hail swath composed of hail streaks from three overlapping radars is shown in Fig. 2a. We conservatively (relative to prior studies, e.g., Soderholm et al. 2017a; Warren et al. 2020; Cintineo et al. 2012) limit swaths to a radial range of 20–140 km in our analysis to mitigate an underestimation of the true hail frequency due the radar's scanning geometry (cone of silence and beam broadening). This conservatism is justified for the Australian radar archive, given the varying beam widths (between 1° and 2° , refer to Table B1) and the dual-PRF artifacts present beyond 140 km. A preliminary analysis of the range dependency of hail frequencies (not shown here) revealed that hail frequencies were relatively stable between our chosen range thresholds and no obvious underestimation was observed for radars with larger beam widths. We direct the reader to Bunkers and Smith (2013) for a more comprehensive discussion of these effects.

Hail streaks from individual radars are then merged by taking the geometric union of spatiotemporally overlapping polygons (refer to Figs. 2a,b), yielding spatially uniform, merged hail swaths. Merged hail streaks are assigned a range of statistics, including their area, start and end times, and optical flow velocities. Most of these statistics require an object-based approach, as they may not be easily calculated from an accumulated, gridded field (Nisi et al. 2018). The resulting merged hail archive (e.g., Fig. 2c), along with the associated object-based statistics, form the basis of our national and regional hail climatologies.

c. Frequency normalization

The precise areal definition of hail streaks in our object-based approach permits a novel, resolution-invariant method for calculating yearly or monthly hail frequencies. In a traditional approach using temporally accumulated (e.g., daily) MESH grids, hail frequencies can be evaluated at the original grid resolution by counting the number of times each pixel exceeds a mesh threshold (e.g., Cintineo et al. 2012). However, by chance, some isolated grid points may not experience a single hailstorm throughout the archive duration, leading to the spurious claim that the true climatological frequency at that

point is zero. One may attempt to account for the finite archive duration by applying various ad hoc smoothing techniques (e.g., Cintineo et al. 2012; Murillo et al. 2021), or calculating hail frequencies on a coarser spatial grid. Hail frequencies calculated using the latter approach (e.g., on a 10-km grid in Warren et al. 2020) yield higher values, as the number of hail detections within a 100-km² area is predictably greater than the number at each individual grid point. This resolution bias in hail frequencies prohibits reliable comparisons between studies with different grid sizes (e.g., Soderholm et al. 2017a; Warren et al. 2020), and confuses the true meaning of hail frequency estimates.

In this study, we define hail frequency as the number of times hail is expected at any single point within a grid box, per normalization period (e.g., yearly or monthly). We justify this choice as more intuitive to an observer, as it attempts to answer the common question: "How many times per year are you likely to observe hail?" This is distinct from: "How many times per year will it hail within 10 km from here?" This spatially invariant hail frequency is calculated by intersecting all hail streaks with a spatial region defined at any resolution. The cumulative area of all hail streaks within that region is then normalized by the area of the region (A) and its radar coverage duration (N , with quality controlled days removed). Formally, hail frequencies (f_h) are defined for each region as follows:

$$f_h = \frac{365.25}{N} \times \frac{\sum_{i=0}^n A_i}{A}, \quad (3)$$

where A_i is the area of the intersection between the i th of n hail streaks and the analysis region. Note that for monthly frequency calculations, 365.25 is replaced by $365.25/12 = 30.4375$, and N and A_i only count days and hail streaks that occur within that month.⁴ This approach can also be applied to gridded hail climatologies by counting the number of MESH grid values that surpass the threshold, before normalizing by the total number of grid points within the coarser climatology grid.

The irregular shape of overlapping radar coverage domains (see, for instance, Fig. 2a for three radars) further complicates the specification of hail frequencies in a regular grid. In grid boxes with overlaps in coverage, it is difficult to prescribe an N value, as different regions within the grid box have been observed for different periods of time. This is especially true for larger grid boxes, such as the 100 km \times 100 km grids illustrated in Fig. 2d. The solution is to intersect the radar coverage geometries with the underlying climatology grid, producing irregular "coverage regions," each with a unique coverage duration. Hail swaths are then intersected with the coverage regions (black lines in Figs. 2d–f), and an individual hail frequency is calculated for each coverage region according to Eq. (3). The result of these region-based frequency calculations is illustrated in Fig. 2e. Finally, we aggregate all region-based frequencies within each grid cell by preferentially weighting those

⁴ Also note that "normalized months" (i.e., 12 months spaced evenly across the year) are used in favor of calendar months to account for the effects of varying month lengths.

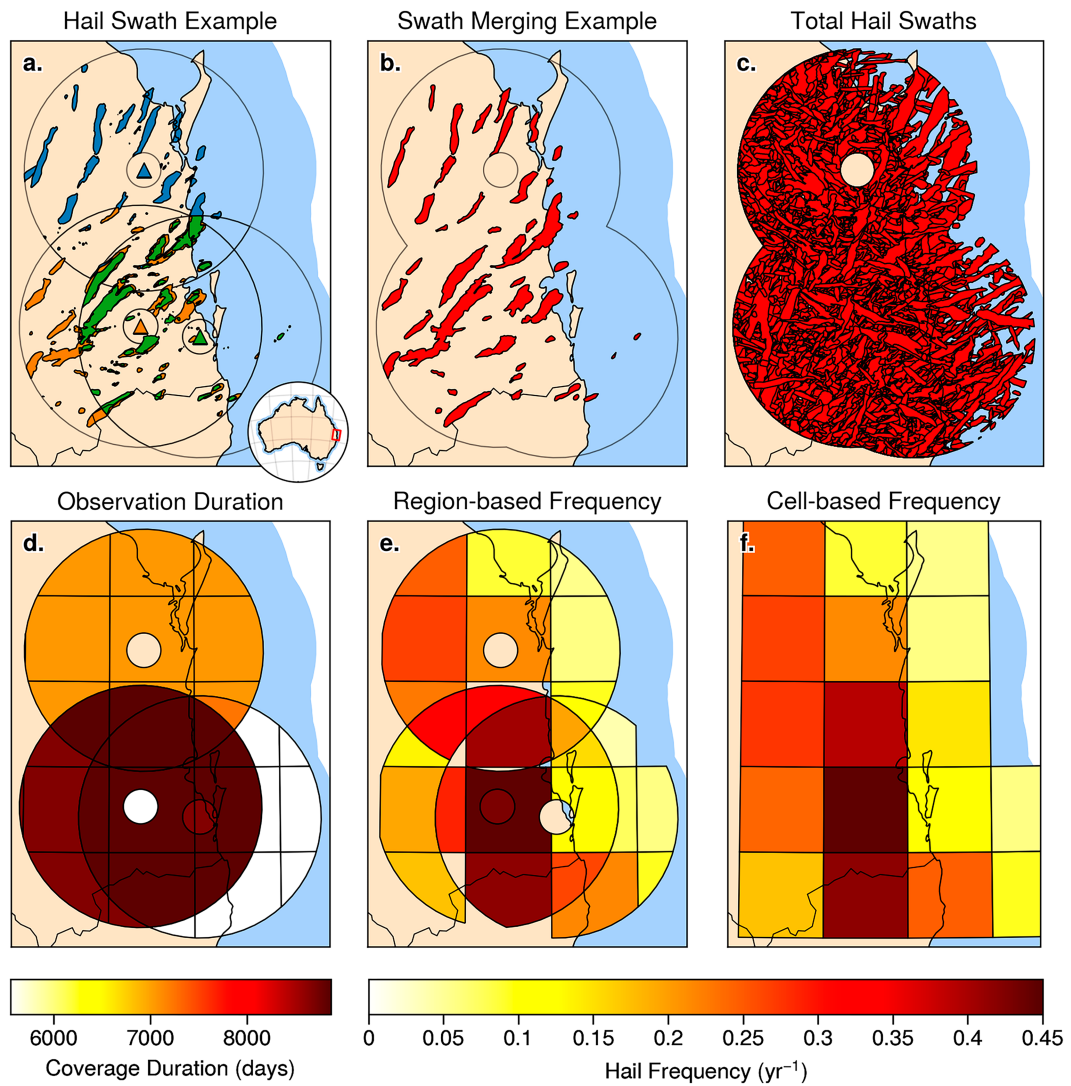


FIG. 2. An illustration of the methods used to calculate the spatially invariant hail climatology. (a) Hail swaths outlined by the 30-mm MESH contour for the Mt. Stapylton (green), Marburg (orange), and Gympie (blue) radars on 16 Dec 2010; (b) merged hail swaths for the same case study (red); and (c) merged hail swaths for the entire archive. The number of days observed for each coverage region at (d) 100-km grid spacing, (e) annual hail frequencies for each coverage region, and (f) cell-based hail frequencies for a uniform grid.

regions with larger areas, longer archive durations, and more overlapping radars (R), as these factors all reduce uncertainty in the underlying frequency estimates. Weighted averages are computed as follows:

$$f_h = \frac{\sum_{j=0}^m (f_{h,j} A_j N_j R_j)}{\sum_{j=0}^m A_j N_j R_j}, \quad (4)$$

where subscripts denote values for the j th of m coverage regions within each grid cell. In this manner, we are able to produce resolution-invariant gridded hail frequencies.

d. Variational interpolation

The Australian radar network covers roughly 30% of the country's land surface, the distribution of which is illustrated in Fig. 1. As a result, some form of interpolation is required to create a continuous hail climatology throughout the country. This interpolation problem is particularly challenging due to large data voids, local variability in hail frequencies, and data noise introduced by the finite sampling period of the archive. Variational inverse methods are well suited to such a problem, as certain "prior knowledge" may be formally introduced to regularize an initially ill-posed system (e.g., Barth et al. 2014). Here, we seek to establish the following assumptions to help constrain the problem at hand:

- 1) Radar-derived hail frequencies are a noisy but representative sample of the true climatological values.
- 2) The true climatological hail frequency varies smoothly in space and time at our chosen resolution.
- 3) No local extrema lie within data voids, and gaps are sufficiently constrained by the surrounding data.
- 4) Hail frequencies reduce to zero at some distance from the coast.

We will briefly discuss the reasoning behind each of these assumptions before outlining their mathematical implementation. First, we justify the representativeness of our frequency estimates in assumption 1 by noting the relative length of our archive (average ~ 17 years, appendix B) compared with semi-national radar-based climatologies [e.g., four years in Cintineo et al. (2012) and eight years in Warren et al. (2020)]. We choose suitably sparse grid spacing to satisfy assumption 2 (100 km), which theoretically dampens high frequencies in the input data through spatial averaging and permits the use of smoothing constraints to “spread” valid information into data voids. Prior studies of the hail climatology in Australia (e.g., Allen and Allen 2016; Bedka et al. 2018; Prein and Holland 2018), provide justification for assumptions 3 and 4, where hail hot-spots are not expected outside the current radar coverage or significantly out to sea. The extent to which the available data constrains the analysis within data voids will be investigated more thoroughly below.

We choose to perform the interpolation iteratively at two spatial scales: first at 200-km resolution to produce a provisional field, then at the final 100-km resolution using the former as a background field (φ_b). This type of nested analysis is common in variational problems (e.g., Laroche and Zawadzki 1994; Dahl et al. 2019), and is useful in our case as valid data spreads more readily at a coarser resolution, providing a useful background for the final analysis. The cost function used in both cases is as follows:

$$\min_{\varphi} \{ \|f_h - \mathcal{R}\varphi\|_2^2 + J_s(\varphi) + J_d(\varphi) + J_b(\varphi, \varphi_b)\}, \quad (5)$$

where φ is the interpolated hail frequency field, \mathcal{R} is a restriction operator that samples the analysis field at data locations, and the standard ℓ_2 norm notation is used throughout the text $\|x\|_2^2 = \sum_{i=1}^N x_i^2$. The second term in the cost function is a second-order smoothing constraint, implemented as follows:

$$J_s(\varphi) = \lambda_s (\|\varphi_{yy}\|_2^2 + \|\varphi_{xx}\|_2^2), \quad (6)$$

where λ_s is a weighting constant and double subscripts denote second-order partial derivatives, e.g., $\varphi_{xx} = (\partial^2 \varphi / \partial x^2)$. Second-order smoothing constraints lead to a visually pleasing minimum curvature solution, and the three-point, centered, finite difference stencil helps spread valid data into data voids (Briggs 1974; Shapiro et al. 2009).

Although J_s may partially remove speckle noise from the frequency data, Brook et al. (2022) found that this constraint alone is unsuitable for denoising due to unwanted by-products produced when heavily weighting this constraint (oversmoothing and extraneous inflections in data voids, Shapiro et al. 2010; Brook et al. 2022). Complementary inclusion of an additional

anisotropic total variation denoising constraint (Rudin et al. 1992) was found to adequately denoise the data, while damping extraneous inflections within the data voids and retaining high amplitude peaks within the analysis fields (refer to appendix B in Brook et al. 2022). The denoising constraint is as follows:

$$J_d(\varphi) = \lambda_d (\|\varphi_y\|_1 + \|\varphi_x\|_1), \quad (7)$$

where λ_d is a weighting constant, subscripts indicate first-order partial derivatives [e.g., $\varphi_x = (\partial \varphi / \partial x)$], and the ℓ_1 norm notation denotes $\|x\|_1 = \sum_{i=1}^N |x_i|$. Forward difference derivatives are used by convention (Rudin et al. 1992).

Finally, the background penalty helps constrain regions outside the data coverage by penalizing deviations from an imposed background field (φ_b). At the provisional resolution (200 km), the background field is uniformly zero and only applies to grid points over the ocean through the application of a weighting matrix that increases exponentially from 0 over land to 1 out to sea ($W_b = \exp(-r^2/d^2)$) where d is the distance from the coast and $r = 400$ km controls the rate of weight increase). At the final resolution, the provisional retrieval is used as the background field, and W_b is then set to 1 for grid points over land with no valid data. Formally, the background constraint is implemented as follows:

$$J_b(\varphi, \varphi_b) = \lambda_b \|W_b(\varphi - \varphi_b)\|_2^2, \quad (8)$$

where λ_b is once again a weighting constant. This constraint serves a dual purpose: it constrains the analysis to zero around the borders of the domain to prevent any extraneous inflections or boundary effects, and assists in filling large data voids with values from the provisional analysis, permitting the use of less aggressive smoothing constraints to prevent oversmoothing.

The aforementioned data voids may lead some readers to question the extent to which the surrounding data actually constrains the interpolated values within. In an attempt to satisfy these concerns and justify assumption 3, we apply the “clever poor man’s error” technique, which is an efficient method for assessing data coverage in variational interpolation problems (Troupin et al. 2012; Beckers et al. 2014). The procedure takes place as follows: set all available data to unit values, reduce the weighting constants by a context-specific factor, and perform the analysis as normal. Due to the difficulties involved in prescribing an exact covariance function for our interpolation procedure, we assume Gaussian covariance and consequently reduce the weights in the second step by a factor of $\sqrt{2}$ (Beckers et al. 2014). The resulting field approximates the “error reduction factor” (i.e., the extent to which the available data reduces analysis errors below background error state), where values close to one indicate the problem is well constrained by the data.

We treat the provision of weighting constants in Eqs. (6)–(8) as a parameter tuning problem (e.g., Brook et al. 2022, 2023). Suitable weights are derived experimentally and ultimately determine the relative strength of each constraint. The chosen values for our interpolation problem are as follows: $\lambda_s = 0.5$, $\lambda_d = 0.01$, and $\lambda_b = 2$. The split Bregman optimization algorithm is used to minimize Eq. (5) due to its

applicability for mixed ℓ_1 - ℓ_2 norms (limited to 5 inner, and 10 outer iterations; Goldstein and Osher 2009; Ravasi and Vasconcelos 2020).

3. Radar frequency correction

A major limitation of the approach outlined in section 2 is the utilization of C- and S-band radars in the Australian archive (wavelengths ~ 5 and ~ 10 cm, respectively). MESH was developed using only S-band radars from the U.S. WSR-88D radar network, and several theoretical challenges arise when attempting to apply it to C-band radars. One primary concern is the increased signal attenuation due to hail at C band (Battan 1971), causing the observed reflectivity (and subsequent MESH values) to diminish relative to S band. Various correction techniques have been proposed for attenuation at C band (e.g., Gu et al. 2011); however, they require polarimetric data and undercorrect hail-induced attenuation (Borowska et al. 2011). To the authors' knowledge, no single-polarized hail attenuation correction exists and thus none is implemented in this study. Instead, we aim to indirectly account for attenuation in a climatological sense using the corrections that follow,⁵ while acknowledging the inevitable loss of information at C band.

The second major methodological challenge in implementing MESH at C-band arises due to non-Rayleigh scattering. Both theoretical scattering calculations (e.g., Ryzhkov et al. 2013) and observational studies (Kaltenboeck and Ryzhkov 2013) indicate that complex scattering effects from hail are more prominent at C band, reducing the reflectivity response relative to S band. Recently, Cecchini et al. (2022) refit the original Z - \dot{E} relationship [Eq. (1), Waldvogel et al. 1978, hereafter W78] at both C and S bands using updated mass/terminal velocity relationships, while also considering the nonsphericity, varying density and complex scattering effects of natural hailstones. Their analysis confirmed that \dot{E} is strongly modulated by the frequency of the illuminating radar, as C-band radars are less sensitive to large hail. However, since the MESH formulation and thresholds used for hail detection (see Table 1) have been developed using the W78 relationship, these updated and likely more accurate relationships may not be directly applied in our analysis. This would require refitting the empirical SHI-MESH function and hail detection thresholds using hail reports (e.g., Murillo and Homeyer 2019), which is outside the scope of our study. Instead, we attempt to generate a C-band analog for the W78 relationship, which aims to account for the aforementioned frequency biases at C band while remaining compatible with the existing MESH formulation.⁶ C-band MESH may be of lower

⁵ We differentiate between a correction made on a climatological basis (which aims to offset the net climatological difference between C- and S-band radars) and one that aims to correct attenuation effects for individual cases.

⁶ The empirical C-band analog of the W78 relationship derived here should not be compared directly to the C-band Z - \dot{E} relationship derived in Cecchini et al. (2022) due to the aforementioned methodological additions in their study. Future work should aim to assess whether their theoretical improvements result in more accurate hail size estimates at both C- and S-band when compared to hail reports.

quality due to the reduced information content; however, previous studies have shown that it remains a skillful hail discriminator (Kunz and Kugel 2015; Skripniková and Rezáčová 2014; Stržínař and Skok 2018). The empirical correction procedure we apply in our study ensures that frequency-related biases are optimally mitigated between C- and S-band radars.

To establish our empirical correction, we examine six regions in the Australian archive with overlapping C-S-band coverage (illustrated in Fig. 3a). These regions were selected from the set of all C-S-band overlaps (refer to Fig. 1) due to their sufficient overlapping coverage area (>4000 km 2) and number of co-sampled hail events (>100). The fitting procedure involved extracting time pairs where the C- and S-band radars both observed MESH > 10 mm within the overlapping observation region, separated by a delay of less than 2 min to ensure temporal proximity. The 10-mm MESH threshold was selected to include events that may be initially underestimated by the C-band radars but could be incorporated into the 30-mm hail archive after correction. Once co-sampling times were identified, all reflectivity data above the 0°C isotherm (i.e., only reflectivities that contribute to MESH) were extracted for columns exceeding the 10-mm MESH threshold, and the nearest pixels were matched between C and S bands for analysis. The precorrection reflectivity fits for each region are shown in red in Figs. 3b–g, confirming the theoretical considerations discussed earlier: C bands underestimate hail reflectivities compared to S bands. Encouraged by the aforementioned frequency-dependent fits developed by Cecchini et al. (2022), we attempt to derive a similar correction empirically by linearly fitting observed reflectivities from the two frequency bands in an attempt to normalize the hail size estimates between them. As we aim to apply a single correction for all C-band radars in the archive (Fig. 3h), we combine the C- and S-band reflectivities for all six analysis regions and apply an iterative orthogonal linear regression technique to arrive at the following corrections:

$$Z_S = 1.113Z_C - 3.929, \quad (9)$$

$$\dot{E} = 2.34 \times 10^{-6} \times 10^{0.093Z_C}, \quad (10)$$

where Eq. (9) was substituted into the original W78 hail kinetic energy relationship [Eq. (1)] to derive its empirical C-band analog in Eq. (10). The chosen fitting technique and additional methodological considerations are outlined in appendix A.

To illustrate the effectiveness of the reflectivity correction in Eq. (9), it is applied to C-band data in each of the overlapping C- and S-band coverage regions, resulting in the 2D histograms shaded in Figs. 3b–h. Visual inspection of these histograms, along with the postcorrection fits (magenta lines), reveal that the correction improves the negative bias for C-band reflectivity for all regions. Quantitatively, the mean bias improved from -2.0 to -0.4 dB for the total data, with the corresponding statistics for each region annotated on each panel. For reference, the precorrection bias of -2 dB corresponds to a $\sim 20\%$ underestimation of MESH values at C band (Warren et al. 2020). Substantial spatiotemporal overlaps in Sydney (Australia's largest city) mean that the

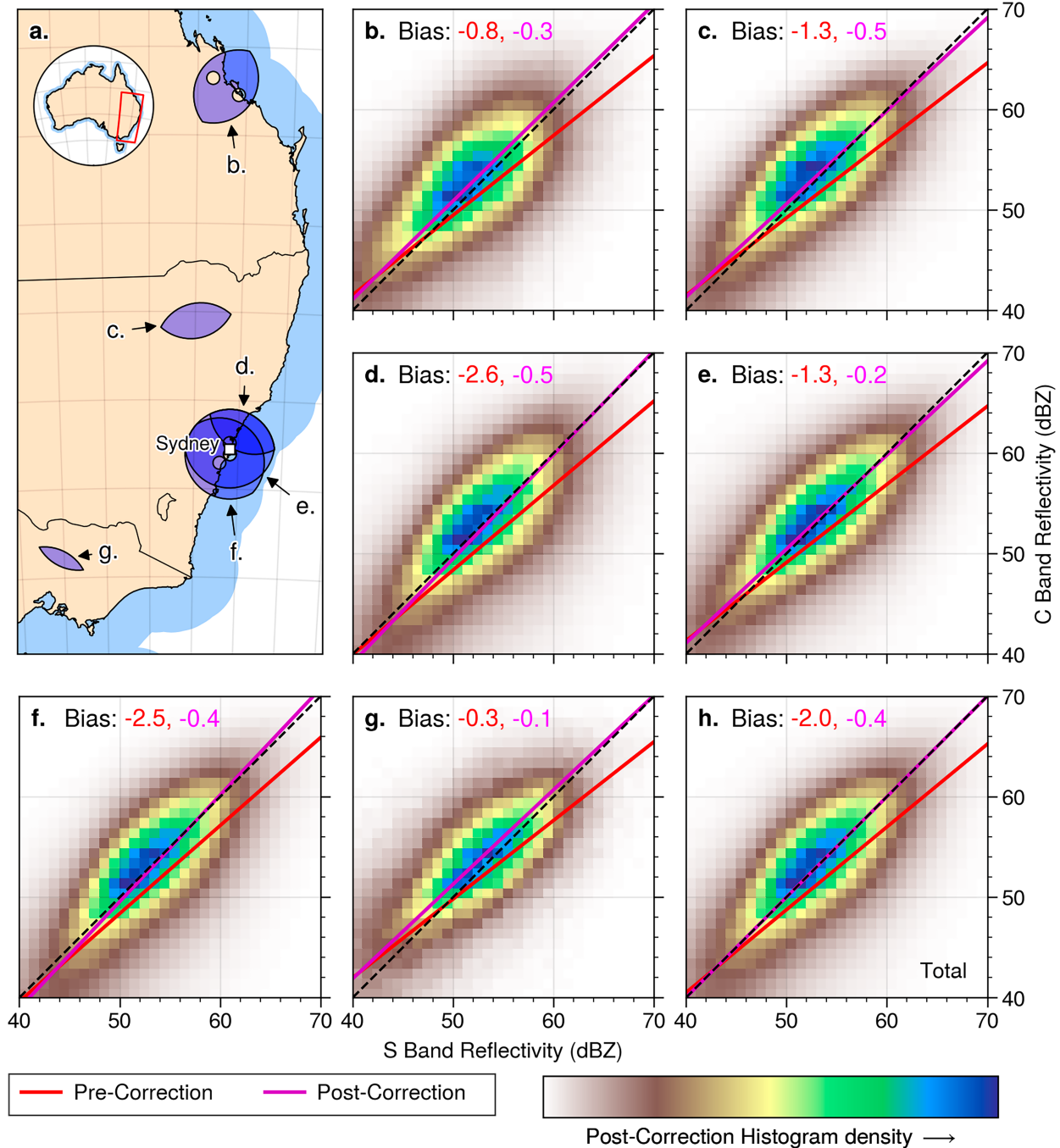


FIG. 3. An illustration of the hail reflectivity fitting process employed in this study. (a) Selected C- and S-band radar overlaps on the east coast of Australia, with labels indicating the panel in which the resultant data are shown. (b)–(g) Data fits for each region, including the precorrection fit between C- and S-band hail reflectivity (red), the corresponding postcorrection fit (magenta), and annotations showing the respective fit biases. A 2D histogram for the postfit reflectivity data is included in each panel, shaded by qualitatively higher data densities. (h) As in the regional overlap panels, but for all data combined.

Kurnell/Woollongong (Fig. 3e) and Kurnell/Terrey Hills (Fig. 3f) overlaps account for $\sim 41\%$ and $\sim 29\%$ of the 18 million individual reflectivity comparisons in the total fit (Fig. 3h). However, it is encouraging to note that the reflectivity

correction works equally well for regions outside of Sydney that contributed fewer data points. Next, we apply this correction to all C-band radars in the archive, aiming to derive a frequency-agnostic hail climatology.

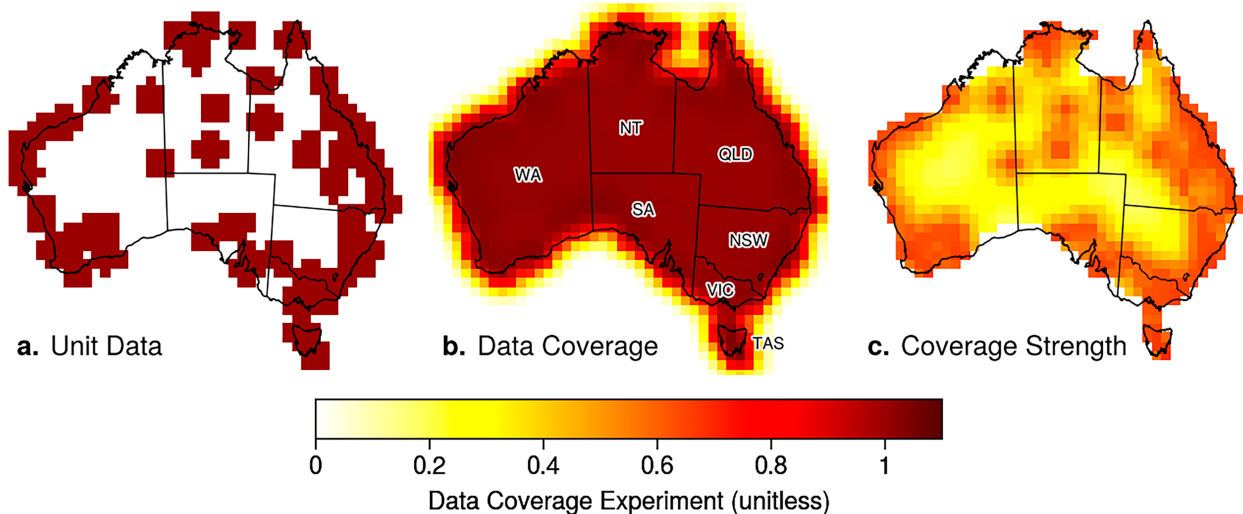


FIG. 4. An illustration of important quantities for interpreting the variational interpolation method used in this study. (a) Data extent of the radar network (filled with unit data according to the poor man's error method). (b) The corresponding poor man's error estimate, a short-hand measure of data coverage. (c) As in (b), but for "strength" of the available radar coverage, refer to text for more details.

4. National climatology

a. Data coverage

We begin our analysis by evaluating how well the available radar data constrains hail frequency estimates in Australia. Figure 4a illustrates the radar network filled with unit data following the "poor man's error" formulation (refer to section 2d). Significant data voids are apparent throughout the country, particularly in central Western Australia (WA), northern South Australia (SA), and western New South Wales (NSW). These areas are devoid of radars due to their sparse population and the fact they largely encompass Australia's deserts. To test whether our interpolation technique is capable of propagating valid information into these voids, the error reduction factor was calculated as outlined in section 2d and shown in Fig. 4b. In general, this quantity is equal to one over land and gradually decreases to zero away from the coastline, where the analysis is dominated by the background constraint and the radar data have minimal impact. The influence of the background constraint also extends slightly inland in regions with no radar coverage along the coastline (e.g., northeast and southeast WA). Such regions are less constrained by the radar data and should be interpreted with this in mind. It is possible to adjust the variational tuning parameters to ensure error reduction factors are close to one everywhere; however, we found that such combinations are prone to oversmoothing. We justify our choice of parameters by noting that the poorly constrained regions are small and that the resulting interpolated fields are a faithful representation of the underlying radar data (e.g., Fig. 5). Error reduction factors being close to unity almost everywhere over land validates our assumption that data voids are adequately constrained at our chosen analysis resolution.

Although Fig. 4b demonstrates that there is sufficient data coverage across the continent, the strength of that data coverage

is highly heterogeneous. To quantify the strength of the data in regions with adequate coverage (error reduction factor > 0.9), we recalculate the error reduction factor for each grid point, this time setting the data at that grid point equal to zero. If the artificial data are placed in a data void, the analysis will be strongly influenced by it and the result will be close to zero. Conversely, if the point is inserted into a data-rich region, the addition of extra data will have less influence, and the result will be closer to one. The resulting field is therefore a quantitative assessment of the strength of radar coverage, with higher values indicating stronger coverage.

Figure 4c reveals that the radar network strongly constrains the analysis around the coast, especially on the east coast. As noted earlier, the interior of the country contains large data voids, and the radar coverage strength is much lower there as a result. Interestingly, the coverage strength is not directly proportional to the distance to the nearest measurement. For example, small radar data gaps in southeast Queensland (QLD) and northeast NSW (Fig. 4a) do not cause a significant drop in this quantity, as they are surrounded by valid data on all sides. In contrast, the coverage strength in western NSW drops immediately when crossing into that data void, as it is unbounded on its northern and western edges. Regions with weaker coverage strength should be assigned lower confidence, as the data are sourced from more distant measurements, and the analysis is more sensitive to measurement errors. The 0.25 coverage strength contour from Fig. 4c is hatched in Figs. 5b and 6 to illustrate the fact that both data coverage and coverage strength should be taken into account when interpreting the subsequent national climatology.

b. Annual hail frequency

Having discussed the intricacies of the chosen interpolation procedure, we present the resulting interpolated hail climatology in Fig. 5. The most notable feature is the broad hail

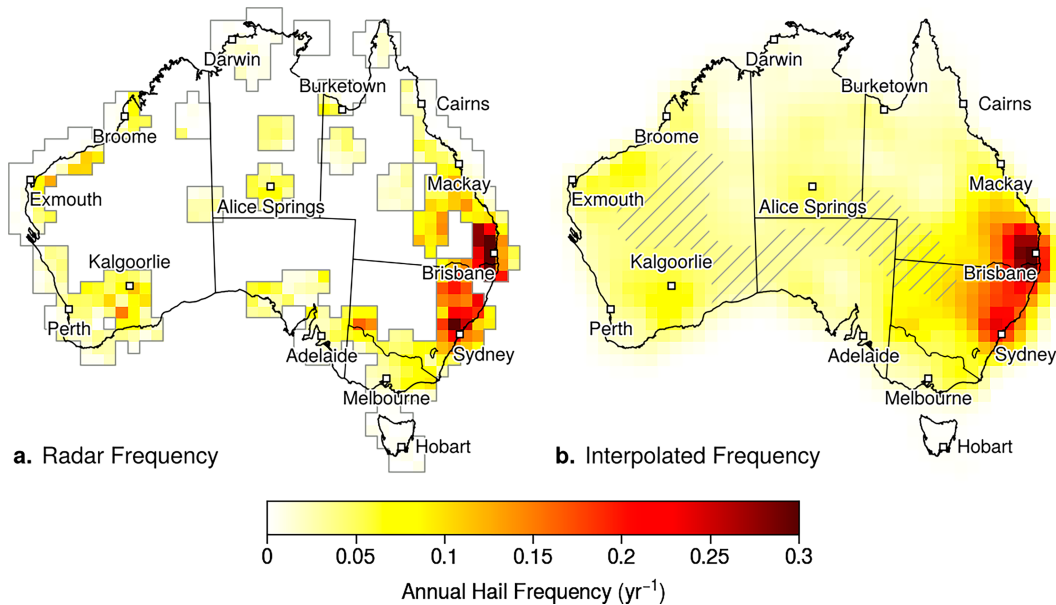


FIG. 5. A national radar-based hail climatology of Australia on a 100-km grid. (a) Climatological hail frequencies calculated using the Australian radar network, with gray outlines illustrating the data extent. (b) Nationally uniform hail frequencies calculated by interpolating the available radar data, with a coverage strength = 0.25 contour hatched in gray.

frequency maximum located on the east coast of Australia, roughly situated south of Mackay in southeast Queensland and north of Sydney in northeast New South Wales. The highest hail frequencies are observed close to the coastline south of Brisbane, proximal to the Great Dividing Range (topography illustrated in Fig. 1). These findings are consistent with previous studies in the Australian region (e.g., Allen and Allen 2016; Bedka et al. 2018). The position and size of this hail-prone region is similar to the hail environment-filtered overshooting top climatology in Bedka et al. (2018), but extends slightly further inland than their study suggests. This inland propagation is partially influenced by a high number of observed events in southwestern NSW [near the SA/NSW/Victoria (VIC) border, Fig. 5a]. Manual quality control affirms the legitimacy of these events, but the frequency disparity compared to the surrounding region suggests that this feature may be a climatological anomaly. Although the interpolation procedure smooths such features toward the “climatological mean,” the anomalous information still propagates into the data void in western NSW. The limited data strength in this region (Fig. 4c), limits our confidence in how far west this hail maximum extends. The recent installation of two radars (Hillston and Brewarrina) largely fills the western NSW radar void and will help alleviate these uncertainties as more data become available in years to come.

Radar-based hail frequencies drop off appreciably south of Sydney, with annual frequencies on the order of 0.05 yr^{-1} across Victoria and southern South Australia. Hailstorms in this region are known to be associated with the passage of frontal systems, which can initiate thunderstorms in otherwise marginal environments. Zhou et al. (2021) demonstrated that

these low instability and moderate to high shear hail environments are dominant in the high latitudes, where cooler temperature profiles also increase the likelihood of hailstones reaching the surface. Previous remote sensing studies have suggested that these relatively shallow hailstorms may result in an underestimation of hail frequencies in southern regions such as Melbourne and Canberra (Bedka et al. 2018; Punge et al. 2018). While there are numerous hail reports in these areas (e.g., Bedka et al. 2018), the reported sizes are smaller on average, reflecting less hail growth due to reduced precipitable water and weaker instability (Allen and Allen 2016). As a result, a greater proportion of hailstorms and hail reports will be correctly overlooked by our 30-mm MESH threshold. It is also possible that MESH is poorly calibrated for detecting large hail due to these structural differences and underestimates the true frequency of hail in southern Australia (having been empirically fit to hail size reports in Oklahoma and Florida, Witt et al. 1998). Future work should investigate the relative accuracy of MESH estimates against hail reports for different high-population centers around the country.

On the west coast, radar coverage is limited to the coastline in the north but extends further inland in the Wheatbelt region between Perth and Kalgoorlie. Both regions exhibit elevated hail frequencies ($>0.1 \text{ yr}^{-1}$), the first along the coastline between Exmouth and Broome and the second in the Goldfields region around Kalgoorlie. Both signatures appear fragmented in the observed radar frequencies (Fig. 5a), with disparate frequencies detected at adjacent grid points. Once again, the interpolation procedure tempers isolated high-frequency points to estimate the climatological mean. The result is a broad region of elevated hail frequency from Broome to Exmouth and around

Kalgoorlie. Notably, the latter does not extend to the coastline in the south near Perth, Australia's fourth most populous city. The land-sea contrast is especially apparent on the north coast of WA, where hail frequencies over the ocean are nearly zero, consistent with climatologically high values of convective inhibition (CIN) observed offshore in the region (Riemann-Campe et al. 2009). Other minor hail frequency maxima are observed by radars in central Australia near Alice Springs, and in northwest Queensland. The former region coincides with a collection of hail reports in the Australian Severe Storms Archive (Allen and Allen 2016), although it is not identified in previous studies involving other remote sensing instruments (e.g., Dowdy and Kuleshov 2014; Bang and Cecil 2019). Bedka et al. (2018) did identify a local hail maximum in the goldfields region near the WA/Northern Territory (NT)/SA border; however, this is not mirrored in the radar archive, with the Giles radar west of Alice Springs showing little hail activity. The other local maximum near Burketown is also observed in the lightning climatology record of Dowdy and Kuleshov (2014), and is probably associated with low-level convergence in the Queensland heat low (Sturman and Tapper 1996) and the onshore passage of cloud lines from the Gulf of Carpentaria (Drosdowsky and Holland 1987).

Tropical radars north of Broome and Cairns (latitudes $\sim 18^\circ$ and 17°S , respectively) exhibit minimal hail activity in our analysis, which is noteworthy for two reasons: 1) these findings may represent the first climatological application of MESH at such latitudes, and 2) previous hail climatology methodologies tend to overestimate hail occurrence in the tropics. These methods include satellite brightness temperatures (e.g., Bang and Cecil 2019), overshooting tops (e.g., Bedka et al. 2018) and hail/severe storm proxies (e.g., Prein and Holland 2018). All such methods are sensitive to tall, overshooting clouds in high-instability environments, which occur commonly in the absence of severe surface hail in the tropics. Several complementary factors are likely responsible for the absence of hail in the region. First, vigorous warm-rain processes below the freezing level are thought to simultaneously limit the amount of supercooled liquid water and increase the number of competing hail embryos in the hail growth zone (Cotton et al. 2010). Second, the lack of wind shear in the tropics (e.g., Allen and Allen 2016; Zhou et al. 2021) means that hail-producing storms are comparatively shorter lived, as outflows from mature cells disrupt their own inflows (May et al. 2002). These structural differences likely reduce the potential updraft residence time, which is critical for hail growth (e.g., Kumjian et al. 2021).

Both structural and microphysical limitations discussed here dictate that hail observed aloft is mostly small ($1\text{--}2\text{ cm}$, May et al. 2002), and likely melts before reaching the surface due to typical temperature profiles in the tropics (Foote 1984). To the contrary, Bang and Cecil (2021) demonstrated that spaceborne Ku-band radar reflectivity profiles are mostly consistent across tropical and subtropical hailstorms identified using different passive microwave detection methods. We propose that this discrepancy arises due to complex scattering and attenuation at Ku-band radar frequencies, which reduces the reflectivity response for larger hail sizes relative to S band and limits the information content available for hail size

discrimination (Ryzhkov et al. 2013; Cao et al. 2013). A notable finding in section 3 is the substantial impact of these effects at C-band frequencies, implying even more pronounced consequences at Ku band. Additionally, the results presented here indicate that unlike Ku-band radars, ground-based S-band and corrected C-band radars effectively distinguish larger hydrometeors likely to reach the ground without melting, thereby minimizing the overestimation of hail frequencies in tropical regions. Admittedly, this analysis is limited to the available radar coverage, which excludes most of the Kimberley coast region in northwest Australia (see Fig. 1),⁷ where other remotely sensed hail (e.g., Bang and Cecil 2019) and severe storm climatologies (e.g., Dowdy and Kuleshov 2014) notably highlight as a hotspot. However, based on the findings in section 4a, we expect that the available radar data adequately constrains hail frequency estimates across tropical Australia. The ground-radar-based assessment of tropical hail frequency shown here appears realistic when compared to Severe Storm Archive hail reports (Allen and Allen 2016) and aligns quantitatively with a 20-yr climatology compiled from press reports by the Queensland Regional Meteorological Office (Frisby and Sansom 1967), with the 1-in-10 year (0.1 yr^{-1}) and 1-in-20 year (0.05 yr^{-1}) isolines terminating around Mackay and Cairns, respectively.

c. Hail seasonality

The final result presented in this section concerns the seasonality of the Australian hail climatology. Figure 6 presents interpolated monthly hail frequencies, calculated using normalized months to ensure an even sample size for each month. Segmenting the historical archive in this manner naturally limits the data available for each interpolation, potentially challenging our assumption that the observed data are a sufficiently representative sample of the actual climatological hail frequency. These limitations can lead to “patchy” hail frequencies for months such as November and February (Figs. 6e,h, respectively), which appear to be affected by climatological anomalies that arise due to the limited duration of the archive. We proceed in discussing the seasonal climatology with these limitations in mind.

While some hail activity is observed on the east coast as early as September, the hail season begins in earnest in October. Early season events are mostly concentrated in southern Queensland and progressively move south as the season advances. Note that the gap observed between Brisbane and Sydney in December and January likely reflects the lack of radar observations in the region (Fig. 5a). By February, the east coast hail frequency maximum has shifted south to around Sydney, showing a steady poleward trend in the intervening months. This aligns with global satellite observations made by Zhou et al. (2021), who suggested that the poleward shift coincides with increases in temperature and moisture at higher latitudes throughout the summer. Locally, Allen and Karoly (2014) and Warren et al. (2020) showed how these effects lead to a poleward shift in instability as the

⁷ An important exception is the Broome radar that covers the Dampier Peninsula on the western fringe of the Kimberleys.

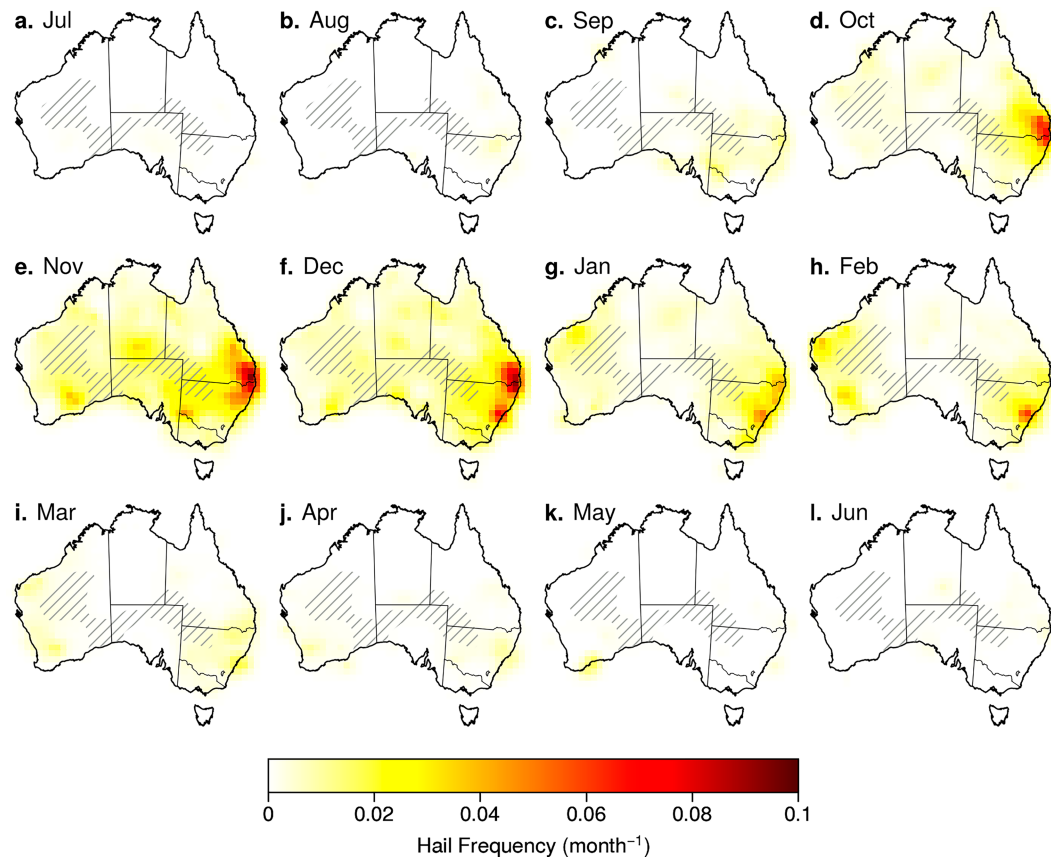


FIG. 6. Interpolated monthly hail frequencies derived from the Australian radar archive on a 100-km grid with a coverage strength = 0.25 contour hatched in gray. Months are normalized into 12 equally spaced periods and are displayed centered on the austral summer.

Austral summer progresses, particularly along the east coast. Conversely, the weakening of lapse rates in the absence of favorable upper-level support results in an overall reduction in hail-producing instability/shear environments in Queensland as the summer progresses (Allen and Karoly 2014; Warren et al. 2020). As a result, the seasonal cycle is comparatively broader and later in NSW (November–March), a finding that is also reflected in hail reports from greater Sydney (Schuster et al. 2005).

Outside the east coast maximum, hail frequencies increase markedly throughout the country in November. This timing coincides with the arrival of continental heat troughs and their associated moisture transport to much of inland Australia (Sturman and Tapper 1996; Hung and Yanai 2004). This moisture, along with suitable upper-level support during late spring or early summer, provides favorable conditions for hail activity in those months, reminiscent of the seasonal climatology of convection in the Great Plains of the United States (Fabry et al. 2017). Under this hypothesis, the collective reduction in hail activity in January–February is a result of a warmer upper atmosphere as the summer progresses. Allen and Karoly (2014) also cited the importance of inland troughs in mid- to late summer for storm development across inland WA. Hailstorms on the west coast of the country remain subdued until later in the season around February, consistent

with the overshooting top-based climatology of Bedka et al. (2018). It is also worth noting that the only major hailstorm to impact the southwest capital city of Perth occurred similarly late in the season (March 2010, Buckley et al. 2010). Hailstorms persist in southern WA later than most of the country, likely due to their association with strong frontal systems that are capable of triggering hailstorms well into Autumn in the absence of strong instability (Allen and Karoly 2014).

5. Regional analysis

Having presented the national climatology in section 4, five regions of interest were identified for further investigation in this section. These regions were selected based on the discussion in section 4 (e.g., northwest Australia and the Goldfields region) and their significance as population centers (e.g., Brisbane and Sydney). We have increased the spatial resolution of the regional climatologies to a 10-km grid; however, this is limited to areas within radar coverage in the absence of spatial interpolation.

The first region of interest is situated in northwest Australia, encompassing the Broome and Port Hedland radars. The high resolution climatology in Fig. 7a reveals a pronounced land–sea contrast, with elevated hail frequencies beginning

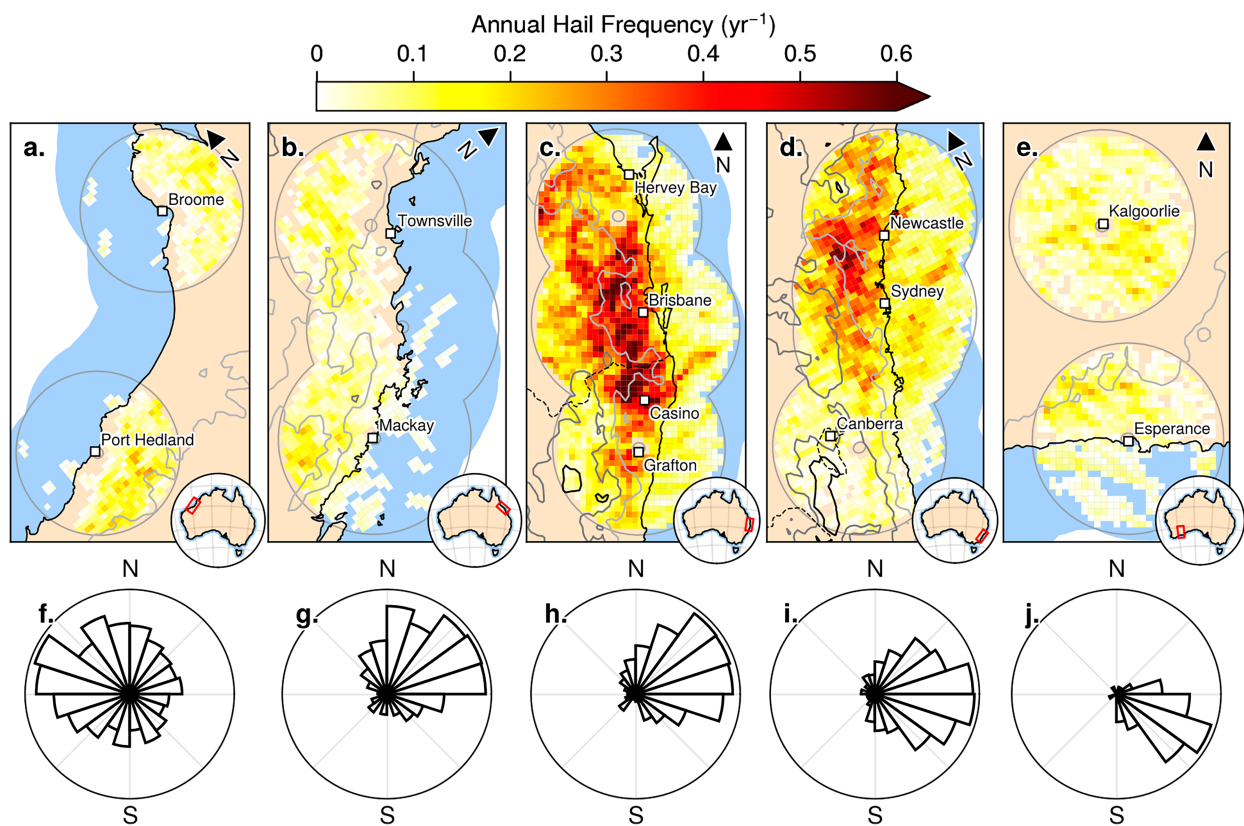


FIG. 7. Regional hail climatologies from five regions of interest. (a)–(e) Hail frequencies direct from the radar data on a 10-km grid (no interpolation), for the northwest Australia (NWA), North Queensland (NQ), Brisbane, Sydney, and southwest Australia (SWA) regions, respectively. Progressively darker gray contours show the 250-, 750-, and 1250-m topography levels, dotted lines represent state/territory borders and circular gray lines illustrate radar coverage extents. Note that (a), (b), and (d) have been rotated for ease of presentation; refer to north arrows and locations in inset panels for orientation. (f)–(j) Rose plots for storm directions in each region (pointing in the direction of storm motion).

roughly 10–30 km inland from the coastline. This highlights the important role of sea breeze circulations for thunderstorm initiation in the tropical Australia (e.g., Carbone et al. 2000; May et al. 2002). The land-sea contrast may also reflect the climatologically high values of CIN offshore (Riemann-Campe et al. 2009) that acts to suppress convection even in the presence of strong low-level convergence (e.g., associated with land breezes; Wapler and Lane 2012). Figure 7f shows that once storms do initiate, most move toward the west, associated with easterly trade winds or monsoon return flow, depending on the time of year. While storms do initiate inland and generally move offshore, Fig. 7a shows that almost all dissipate before reaching the coastline. Figure 8a also shows that hail streaks are, on average, shorter in northwest Australia, further substantiating the ephemeral nature of hailstorms in the region. The seasonal distribution of hailstorms in the region is distinctly bimodal (Fig. 8b), with the break in December coinciding with the average arrival of the monsoon (Hung and Yanai 2004). It is likely that increases in column-integrated moisture and weaker lapse rates associated with the active monsoon suppress hail activity during this period. It remains unclear whether MESH detections are substantiated by hailfall

at the surface in these remote regions due to the extremely low population density. However, the coastal offset illustrated in Fig. 7a may explain why tropical population centers on the coast rarely encounter hail, yet a surprising number of hail reports have been noted in the inland road network in northwest Australia (Allen and Allen 2016).

The second region, located in northeastern Australia at a latitude similar to the first, provides an additional validation source for the characteristics of tropical hailstorms. Figure 7b shows that the overall hail frequency, and spatial offset from the coastline is similar to northwest Australia, albeit with increased offshore activity in the southern parts of the domain. Unlike coastal population centers on the west coast, nonzero hail frequencies extend to the coastline near Mackay, which notably recorded Australia's largest measured hailstone nearby in 2021 (16 cm in diameter, BoM 2021). Figure 7g shows that storms predominantly move offshore toward the northeast, perhaps reflecting the southerly component required for significant instability aloft at these latitudes. These types of systems typically occur in late spring and early summer (section 4), before the monsoon regime draws in tropical air masses from the east later in the season (Sturman and

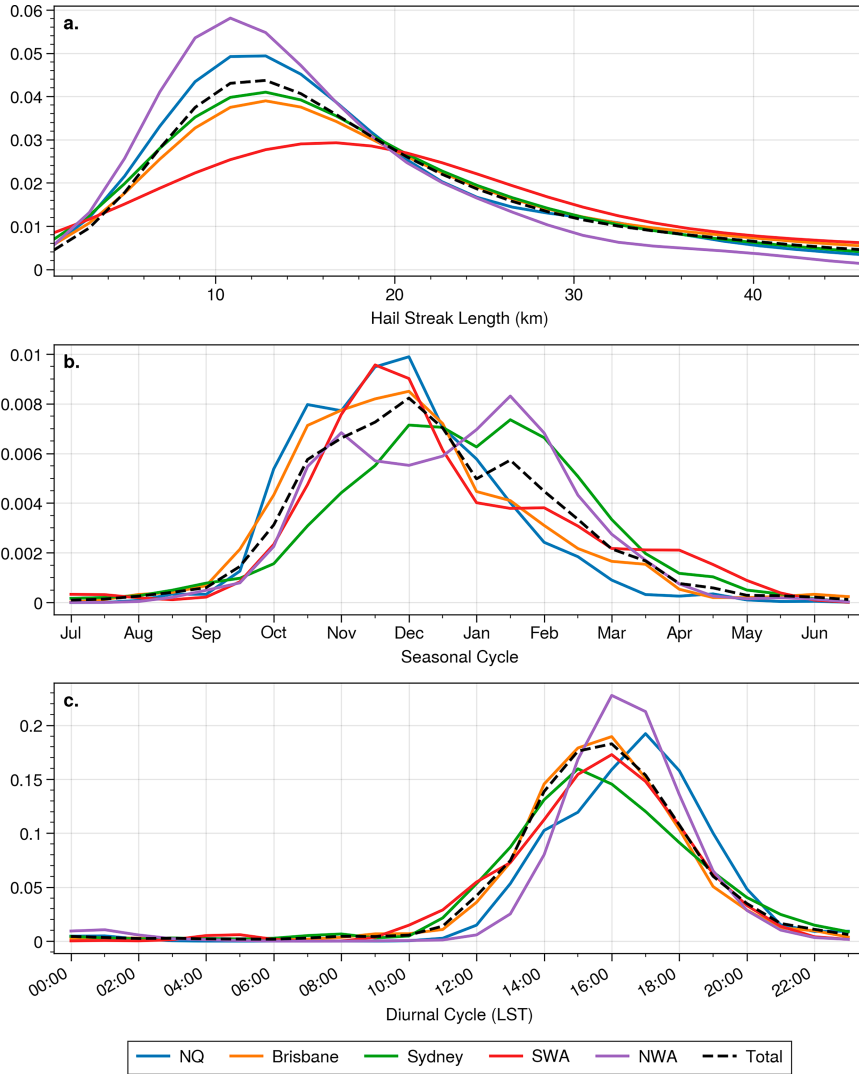


FIG. 8. Normalized probability density functions of hailstorm statistics for the five regions of interest identified in section 5 and the entire archive (total). (a) Length of the hail streak major axis, (b) seasonal cycle measured by hailstorm counts over 24 equally spaced time periods (\sim biweekly), and (c) diurnal cycle measured by hourly counts of active hailstorms measured in local solar time (LST).

Tapper 1996). Figures 8a and 8c also confirm that, similar to the northwest Australia region, these tropical hail events are shorter in length and occur later in the day than their subtropical counterparts. The comparatively late diurnal cycle in the tropics (both northwestern and northeastern regions, usually between 1600 and 1800 local time) is consistent with that of overshooting convection in other locations in northern Australia such as Cairns and Darwin (Bedka et al. 2018).

The next region of interest coincides with the national hail frequency maximum in southeast Queensland/northeast New South Wales. This region contains the highest hail frequencies on the continent, consistent with prior hail climatologies (McMaster 2001; Schuster et al. 2005; Bedka et al. 2018). The maximum hail frequency west of Casino in Fig. 7c also aligns

closely with the regional MESH-based climatology in Warren. It is difficult to compare the maximum frequency values observed [2.5 hail days per year per 100 km^2 in Warren et al. (2020) versus ~ 0.9 hailstorms per year here] due to methodological differences used for frequency estimation in both studies (see section 2c). The highest hail frequencies occur on either side of the QLD/NSW border, which follows the ridge top of the McPherson mountain range. The observed hail maxima along sloping terrain, rather than mountain peaks, is consistent with local thunderstorm initiation hypotheses, including thermally driven valley winds, orographic lifting, and leeward convergence of obstructed flows (Sturman and Tapper 1996; Soderholm et al. 2017a; Nisi et al. 2018; Warren et al. 2020). A secondary hail maximum to the northwest of Brisbane was also

observed by Soderholm et al. (2017a), who hypothesized that storm intensification may be promoted by latent heat fluxes from nearby Lakes Wivenhoe and Somerset. Figure 7h indicates predominantly northeasterly storm motion, consistent with the dominant westerly steering flow in the subtropics and influence of southerly airmasses for high-end thunderstorm events in the region (Soderholm et al. 2019). Previously identified southwest-northeast storm pathways may be identified in Fig. 7c (e.g., from the border ranges toward Brisbane, Soderholm et al. 2017a; Warren et al. 2020), along with a prominent storm pathway off the coast east of Casino.

Hail frequencies are generally concentrated on the coastal plain to the east of the Great Dividing Range in Fig. 7c. Along with the previously mentioned initiation mechanisms, this region is thought to be more favorable for hailstorms due to interactions with sea breezes (which supplement low-level moisture and wind shear), and more localized factors such as added latent heat fluxes from irrigated farmland and urban heat island effects (Soderholm et al. 2017a,b). Accordingly, hail frequencies reduce substantially onto the elevated New England Tableland in northeastern NSW, which is roughly traced by the 750-m elevation contour in Fig. 7c.⁸ Hail frequencies appear to drop spuriously in regions solely covered by the Grafton radar, which is known to display persistently poor calibration and hardware-related insensitivity (M. Curtis 2023, personal communication, Bureau of Meteorology). Despite these issues, Grafton data were included in Fig. 7 to illustrate hail frequencies in a relative sense across northern NSW, due to the region's importance as a climatological hail maximum (see Fig. 5). The Grafton radar was not included in the national climatology ([appendix B](#)) due to these reasons.

The pattern of hail activity along the southern stretches of the NSW coastline, around Sydney, depicted in Fig. 7d is generally similar to that in northeastern NSW. Hailstorms are concentrated on the coastal plain, with a particular prevalence on the eastern slopes of the Great Dividing Range. Hail frequencies appear to diminish atop elevated topography (>750 m), preferring mountain slopes rather than peaks. As a result, hail frequencies drop off considerably in the Snowy Mountains south of Canberra, and more broadly south of Sydney. Schuster et al. (2005) also noted a marked drop in hail reports to Sydney's south, despite the large population density. Figure 7i supports the general picture of hail activity in the region, whereby storms initiate along the ranges to the east, before tracking eastward, intensifying across the coastal plain, and finally dissipating over the ocean (Potts et al. 2000; Schuster et al. 2005; Warren et al. 2020). Oceanic hailstorms appear to be more common in the Sydney region compared to Brisbane (Warren et al. 2020), aligning with the increased prevalence of lightning offshore in the region (Dowdy and Kuleshov 2014).

The final region of interest is the Goldfields region in southwestern Australia (Fig. 7e). The temperate climate and proximity

to the Southern Ocean dictate that strong frontal systems are a dominant driver of storm activity in the region (Sturman and Tapper 1996; Allen and Karoly 2014). As a result of these broad-scale initiation mechanisms, hail frequencies are generally quite uniform spatially, with a less-pronounced land-sea contrast. The southeasterly directions shown in Fig. 7j are consistent with the orientation of prefrontal troughs, which form ahead of Southern Ocean cold fronts roughly twice a month in summer (Hanstrum et al. 1990a). These setups advect warm continental air toward the southeast during their passage across the southern parts of the continent, triggering severe thunderstorms under favorable environmental conditions (Hanstrum et al. 1990a,b), and are commonly responsible for hailstorms across southern Australia (Buckley et al. 2010). Figure 8a also shows the resulting hail streaks in southern WA are notably longer than those in the rest of the country.

6. Summary and future directions

This study aimed to develop a national radar-based hail climatology with a broad focus on the national and regional scales. Challenges unique to the Australian radar archive (e.g., varying radar frequencies and limited spatial coverage) complicated these endeavors, and various methodological advances were required to achieve the objectives of the study. The main methodological contributions outlined in this study are as follows:

- The introduction of an object-based hail processing algorithm enabled the calculation of resolution-invariant hail frequencies, which are more intuitive for individual observers and enable intercomparison between studies.
- A hail reflectivity correction was proposed for calculating maximum estimated size of hail (MESH) estimates at C band, minimizing climatological differences with S bands in the Australian archive.
- A novel variational method for interpolating radar-based hail frequencies across the country was introduced to produce a spatially continuous national hail climatology.

These methodological advances permitted the investigation of hail occurrence across the aforementioned range of spatial scales. First, the hail frequencies were estimated on a national scale in [section 4](#), and showed a broad hail maximum on the east coast of the country between roughly Mackay and Sydney. The radar-based archive indicates that hailstorms occur once every 3–5 years at individual locations on the east coast. Elevated hail frequencies also occur on the northwest coast and inland stretches of southwest Australia, but are less than half as frequent as those on the east coast.

Regional climatologies showed that hailstorms occur most frequently on the eastern slopes of the Great Dividing Range around the Brisbane and Sydney regions (one hail event every ~1–2 years). Tropical hailstorms were found to be shorter in terms of length and initiate later in the day with a strong land-sea contrast. Subtropical hailstorms on the east coast were found to shift poleward throughout the summer, starting in Queensland in November and progressing toward Sydney by March. Finally, temperate hailstorms in southern Australia were observed to produce longer hail streaks and mainly propagate toward the southeast, responding with known synoptic-scale drivers in the region.

⁸ Interestingly, older report-based climatologies indicate that the number of hail reports and crop losses are comparable between the New England Tableland and the coastal plain (McMaster 2001; Schuster et al. 2005), likely a result of their earlier study periods.

During this study, several important avenues for future work were identified. First, secondary data sources, such as hail proxies from weather models or various satellite-based products, should be used to help constrain hail frequency estimates in areas with poor radar coverage, such as western New South Wales. These data sources may be incorporated as an additional background constraint in the variational interpolation method introduced herein. Further research should also investigate the accuracy of MESH for hail identification in different climatic regions such as the tropics and southern Australia, using hail both hail reports and comparisons with satellite-based remote sensing products. These studies should also investigate how storm-driven hail advection, melting, and size sorting can also affect radar-based climatological assessments (e.g., Brook et al. 2021). Finally, future research should also explore how the radar archive may be used to identify long-term trends and interannual/decadal variability previously noted in the Australian hail climatology (Schuster et al. 2005; Allen and Karoly 2014), in the context of how they may be evolving in a changing climate.

Acknowledgments. This research was undertaken with the assistance of resources and services from the National Computational Infrastructure (NCI), which is supported by the Australian government. Author Brook would like to acknowledge Guy Carpenter and Company, LLC for industry funding throughout their postgraduate studies. We also acknowledge Mark Curtis and Valentin Louf for discussions on the Australian Radar Archive.

Data availability statement. Download instructions for all data used in this study may be found in the Australian Unified Radar Archive (AURA; Soderholm et al. 2022) and are available at <https://www.openradar.io/operational-network>. Data processing software is available upon request to the author.

APPENDIX A

Iterative Orthogonal Linear Regression

We expect the reflectivity response of large hail to diminish at C band due the theoretical considerations outlined in section 3. Here, we attempt to correct C-band hail reflectivities to match those at S band, where the chosen hail detection methodology was developed. The fitting procedure used to generate the correction is a linear orthogonal regression. This technique is suitable for our purposes, as it considers measurement error in both x and y variables, which is distinct from an ordinary least squares regression that assumes the x variable is known without error. Orthogonal regression is also suitable for our application due to our use of point-matched values of the same variable, which, due to the identical matching procedure employed to both, we may assume to have equal variance (York 1966). Carroll and Ruppert (1996) show that orthogonal regression may be misused if the ratio of input variable variance is incorrectly specified, or due to nonlinearities in the underlying dataset. Despite these concerns, we consider it an appropriate technique for our case and employ an efficient FORTRAN implementation (Boggs et al. 1989).

The aim is to fit only those reflectivities that correspond to MESH detections, which dictates data are taken from above the 0°C isotherm in columns where MESH exceeds 10 mm (refer to section 3 for a discussion on the 10-mm MESH threshold). We also only use data above 40 dBZ, as in the MESH formulation. Orthogonal regression is used to fit C- and S-band reflectivities as the x and y variables, respectively, resulting in a standard linear function: $y = mx + c$, where m and c are the linear coefficients. When the correction is applied to the y data, the initial fit is transposed as follows:

$$Y_1 = \frac{y_0 - c_1}{m_1}, \quad (\text{A1})$$

where Y denotes the corrected y data, y_0 is the initial y data, and subscripts denote the n th correction. Depending on the sign of the correction, Y_1 may now contain data above or below the 40-dBZ threshold, which should be included or excluded from the fitting calculation, respectively. This problem is analogous to one encountered in radar calibration, where spaceborne reflectivity data above a certain threshold are used to calculate a calibration offset (Protat et al. 2011; Warren et al. 2018). The solution arises by proceeding iteratively, applying the correction and filtering the data according to the threshold at each step. The linear corrections in our case introduce additional complexity (compared to the constant offset used in radar calibration), and we now describe how the final correction may be obtained from the fit at each iteration. Once the 40-dBZ threshold has been applied to Y_1 , we recorrect the data in the second iteration:

$$Y_2 = \frac{Y_1 - c_2}{m_2} = \frac{\frac{y_0 - c_1}{m_1} - c_2}{m_2}, \quad (\text{A2})$$

where Eq. (A1) was substituted in the final expression. The refitting process continues until the difference between the coefficients m and c in consecutive iterations is less than a user-defined convergence criterion (ϵ , where $\epsilon = 1 \times 10^{-4}$ in this study). The resulting correction when applying the refitting procedure for n iterations is generalized below:

$$Y_n = \frac{y_0}{\prod_{i=1}^n m_i} - \sum_{i=1}^n \frac{c_i}{\prod_{j=i}^n m_j}. \quad (\text{A3})$$

The optimization converged in roughly 20 iterations for the fits illustrated in Fig. 3. Although no divergent cases were observed in our analysis, we offer no formal proof of convergence for the method outlined here.

APPENDIX B

Radar Information

In Table B1, we present details of the radars utilized in this study. Key characteristics, including hardware type, beamwidth, and frequency, are documented due to their impact on the quality of hail retrievals.

TABLE B1. Relevant information for radars used in this study. Missing end dates indicate radars were still operational at the end of the study period, altitudes indicate antenna height above sea level, and beam widths are measured in degrees to half-power. Refer to <https://openradar.io/> for further details.

Location	Radar type	Start date	End date	Duration (years)	Lat (°S)	Lon (°E)	Alt (m)	Frequency	Beamwidth (°)
Adelaide (B. Park)	Meteor1500SDP	27 Oct 2005	—	16.2	34.62	138.47	29.0	S	1.0
Adelaide (S. Hill)	WSR81C	1 Jan 2000	—	22.0	35.33	138.50	395.1	C	1.7
Albany	Meteor735CDP	21 Feb 2003	—	18.9	34.94	117.82	93.0	C	1.0
Alice Springs	WF100-6C	28 Oct 2003	—	18.2	23.80	133.89	563.3	C	1.7
Bairnsdale	Wurrung_2502C	6 May 2008	—	13.7	37.89	147.58	65.3	C	1.7
Bowen	WF100-6C	7 May 2004	—	17.7	19.89	148.07	72.5	C	1.7
Brisbane (Marburg)	WSR74S	1 Jan 2000	—	22.0	27.61	152.54	371.1	S	1.9
Brisbane (Mt Stap.)	Meteor1500SDP	8 Jun 2006	—	15.6	27.72	153.24	175.0	S	1.0
Broome	DWSR2502C	18 Mar 2008	—	13.8	17.95	122.24	31.4	C	1.7
Cairns	DWSR2502C	11 Jan 2000	—	22.0	16.82	145.68	660.8	C	1.0
Canberra	DWSR74S	22 Nov 2002	—	19.1	35.66	149.51	1382.7	S	1.9
Carnarvon	DWSR2502C	7 Dec 2004	—	17.1	24.89	113.67	12.0	C	1.7
Ceduna	DWSR2502C	6 Jan 2002	—	20.0	32.13	133.70	32.0	C	1.7
Dampier	WRM200CDP	13 Aug 2009	—	12.4	20.65	116.68	55.0	C	1.0
Darwin (Berrimah)	DWSR2502C	7 Dec 2000	—	21.1	12.46	130.93	60.0	C	1.0
Emerald	DWSR8502S	9 Mar 2010	—	11.8	23.55	148.24	211.3	S	1.9
Esperance	Meteor735CDP	19 Feb 2003	—	18.9	33.83	121.89	42.9	C	1.0
Geraldton	Meteor735CDP	8 Feb 2003	—	18.9	28.80	114.70	47.7	C	1.0
Giles	WF100-5C	15 Oct 2003	—	18.2	25.03	128.30	607.4	C	2.0
Gladstone	WSR74S	1 Jan 2000	—	22.0	23.86	151.26	92.5	S	1.9
Gove	TVDR2500	1 Oct 2002	—	19.3	12.28	136.82	75.7	C	1.7
Grafton	WSR74S	1 Jan 2000	—	22.0	29.62	152.95	49.8	S	1.9
Gympie	DWSR8502S	1 Jan 2000	—	22.0	25.96	152.58	355.0	S	1.9
Halls Creek	WF100-5C	26 Mar 2008	—	13.8	18.23	127.66	439.4	C	1.7
Hobart	DWSR2502C	22 Mar 2012	—	9.8	43.11	147.81	511.7	C	1.0
Kalgoorlie	DWSR2502C	13 Nov 2003	—	18.1	30.78	121.45	390.0	C	1.0
Katherine (Tindal)	WSR81C	15 Oct 2003	—	18.2	14.51	132.45	148.4	C	1.7
Learmouth	TVDR2500	11 Feb 2008	—	13.9	22.10	114.00	333.3	C	1.7
Longreach	WF100-6C	18 Dec 2000	—	21.0	23.43	144.29	201.6	C	1.7
Mackay	TVDR2500	1 Jan 2000	—	22.0	21.12	149.22	43.9	C	1.7
Melbourne	Meteor1500SDP	1 Jan 2000	—	22.0	37.86	144.76	45.0	S	1.0
Mildura	WF100-5C	1 Jan 2002	15 Mar 2021	19.2	34.24	142.09	59.3	C	2.0
Moree	WF100-5C	1 Jan 2000	—	22.0	29.49	149.85	221.5	C	1.7
Mornington Island	WSR81C	1 Jan 2000	—	22.0	16.67	139.17	19.6	C	1.7
Mount Isa	DWSR8502S	14 Sep 2012	—	9.3	20.71	139.56	516.7	S	1.9
N.W. Tasmania	Wurrung_2502C	1 Jan 2000	—	22.0	41.18	145.58	601.0	C	1.0
Namoi	DWSR8502S	2 Jun 2010	—	11.6	31.02	150.19	720.0	S	1.9
Newcastle	DWSR74S	1 Jan 2000	—	22.0	32.73	152.03	84.0	S	1.9
Perth (Serpentine)	TVDR2500	2 Feb 2010	—	11.9	32.39	115.87	39.8	C	1.0
Port Hedland	TVDR2500	12 Mar 2008	—	13.8	20.37	118.63	23.8	C	1.7
Rockhampton	WF100C	1 Jan 2000	31 Aug 2014	14.7	23.38	150.47	14.0	C	1.6
South Doodlakine	Wurrung_2502C	15 Feb 2017	—	4.9	31.78	117.95	416.0	C	1.7
Sydney (Kurnell)	WF100-6C	1 Jan 2000	—	22.0	34.01	151.23	63.8	C	1.0
Sydney (T. Hills)	Meteor1500SDP	15 May 2009	—	12.6	33.70	151.21	223.5	S	1.0
Tennant Creek	WF100C	10 Jul 2007	30 Jun 2015	8.0	19.64	134.18	394.0	C	1.8
Townsville	DWSR2502C	3 Aug 2011	—	10.4	19.42	146.55	612.5	C	1.0
Warrego	TVDR2500	6 Oct 2006	—	15.2	26.44	147.35	534.4	C	1.7
Warruwi	DWSR2502C	15 Nov 2012	—	9.1	11.65	133.38	43.7	C	1.0
Weipa	WF100C	1 Jan 2000	11 Oct 2015	15.8	12.67	141.92	35.0	C	1.7
Wollongong	DWSR8502S	1 Jan 2000	—	22.0	34.26	150.88	471.6	S	1.9
Woomera	WF100-6C	4 Jan 2001	—	21.0	31.16	136.80	175.9	C	1.7
Yarrawonga	WF100-6C	25 Jun 2002	—	19.5	36.03	146.02	146.0	C	1.0

REFERENCES

- Allen, J. T., 2012: Supercell storms: Melbourne's White Christmas 2011. *Bull. Aust. Meteor. Oceanogr. Soc.*, **25**, 47–51.
- , and D. J. Karoly, 2014: A climatology of Australian severe thunderstorm environments 1979–2011: Inter-annual variability and ENSO influence. *Int. J. Climatol.*, **34**, 81–97, <https://doi.org/10.1002/joc.3667>.
- , and M. K. Tippett, 2015: The characteristics of United States hail reports: 1955–2014. *Electron. J. Severe Storms Meteor.*, **10** (3), <https://doi.org/10.55599/ejssm.v10i3.60>.
- , and E. R. Allen, 2016: A review of severe thunderstorms in Australia. *Atmos. Res.*, **178–179**, 347–366, <https://doi.org/10.1016/j.atmosres.2016.03.011>.
- Anagnostou, E. N., and W. F. Krajewski, 1999: Real-time radar rainfall estimation. Part I: Algorithm formulation. *J. Atmos. Oceanic Technol.*, **16**, 189–197, [https://doi.org/10.1175/1520-0426\(1999\)016<0189:RTRREP>2.0.CO;2](https://doi.org/10.1175/1520-0426(1999)016<0189:RTRREP>2.0.CO;2).
- Australian Bureau of Statistics, 2021: Regional population: Statistics about the population and components of change (births, deaths, migration) for Australia's capital cities and regions. Australian Bureau of Statistics, accessed 8 April 2023, <https://www.abs.gov.au/statistics/people/population/regional-population/latest-release>.
- Bang, S. D., and D. J. Cecil, 2019: Constructing a multifrequency passive microwave hail retrieval and climatology in the GPM domain. *J. Appl. Meteor. Climatol.*, **58**, 1889–1904, <https://doi.org/10.1175/JAMC-D-19-0042.1>.
- , and —, 2021: Testing passive microwave-based hail retrievals using GPM DPR Ku-band radar. *J. Appl. Meteor. Climatol.*, **60**, 255–271, <https://doi.org/10.1175/JAMC-D-20-0129.1>.
- Barth, A., J.-M. Beckers, C. Troupin, A. Alvera-Azcárate, and L. Vandenberghe, 2014: Divand-1.0: N -dimensional variational data analysis for ocean observations. *Geosci. Model Dev.*, **7**, 225–241, <https://doi.org/10.5194/gmd-7-225-2014>.
- Battan, L. J., 1971: Radar attenuation by wet ice spheres. *J. Appl. Meteor.*, **10**, 247–252, [https://doi.org/10.1175/1520-0450\(1971\)010<0247:RABWIS>2.0.CO;2](https://doi.org/10.1175/1520-0450(1971)010<0247:RABWIS>2.0.CO;2).
- Beckers, J.-M., A. Barth, C. Troupin, and A. Alvera-Azcárate, 2014: Approximate and efficient methods to assess error fields in spatial gridding with Data Interpolating Variational Analysis (DIVA). *J. Atmos. Oceanic Technol.*, **31**, 515–530, <https://doi.org/10.1175/JTECH-D-13-00130.1>.
- Bedka, K. M., 2011: Overshooting cloud top detections using MSG SEVIRI infrared brightness temperatures and their relationship to severe weather over Europe. *Atmos. Res.*, **99**, 175–189, <https://doi.org/10.1016/j.atmosres.2010.10.001>.
- , J. Brunner, R. Dworak, W. Feltz, J. Otkin, and T. Greenwald, 2010: Objective satellite-based detection of overshooting tops using infrared window channel brightness temperature gradients. *J. Appl. Meteor. Climatol.*, **49**, 181–202, <https://doi.org/10.1175/2009JAMC2286.1>.
- , J. T. Allen, H. J. Punge, M. Kunz, and D. Simanovic, 2018: A long-term overshooting convective cloud top detection database over Australia derived from MTSAT Japanese Advanced Meteorological Imager observations. *J. Appl. Meteor. Climatol.*, **57**, 937–951, <https://doi.org/10.1175/JAMC-D-17-0056.1>.
- Bednarczyk, C. N., and P. J. Sousounis, 2012: Hail climatology of Australia based on lightning and reanalysis. *27th Conf. on Severe Local Storms*, Madison, WI, Amer. Meteor. Soc., 142, https://ams.confex.com/ams/27SLS/webprogram/Manuscript/Paper255889/extendedAbstract_pdf.pdf.
- Boggs, P. T., J. R. Donaldson, R. Byrd, and R. B. Schnabel, 1989: Algorithm 676: ODRPACK: Software for weighted orthogonal distance regression. *ACM Trans. Math. Software*, **15**, 348–364, <https://doi.org/10.1145/76909.76913>.
- BoM, 2021: Bureau of meteorology severe thunderstorm archive. Australian Bureau of Meteorology, accessed 21 June 2023, <http://www.bom.gov.au/australia/stormarchive/>.
- Borowska, L., A. Ryzhkov, D. Zrnić, C. Simmer, and R. Palmer, 2011: Attenuation and differential attenuation of 5-cm wavelength radiation in melting hail. *J. Appl. Meteor. Climatol.*, **50**, 59–76, <https://doi.org/10.1175/2010JAMC2465.1>.
- Briggs, I. C., 1974: Machine contouring using minimum curvature. *Geophysics*, **39**, 39–48, <https://doi.org/10.1190/1.1440410>.
- Brook, J. P., A. Protat, J. Soderholm, J. T. Carlin, H. McGowan, and R. A. Warren, 2021: HailTrack-improving radar-based hailfall estimates by modeling hail trajectories. *J. Appl. Meteor. Climatol.*, **60**, 237–254, <https://doi.org/10.1175/JAMC-D-20-0087.1>.
- , —, J. S. Soderholm, R. A. Warren, and H. McGowan, 2022: A variational interpolation method for gridding weather radar data. *J. Atmos. Oceanic Technol.*, **39**, 1633–1654, <https://doi.org/10.1175/JTECH-D-22-0015.1>.
- , —, C. K. Potvin, J. S. Soderholm, and H. McGowan, 2023: The effects of spatial interpolation on a novel, dual-Doppler 3D wind retrieval technique. *J. Atmos. Oceanic Technol.*, **40**, 1325–1347, <https://doi.org/10.1175/JTECH-D-23-0004.1>.
- Buckley, B. W., W. Sullivan, P. Chan, and M. Lepastrier, 2010: Two record breaking Australian hail storms: Storm environments, damage characteristics and rarity. *25th Conf. on Severe Local Storms*, Denver, CO, Amer. Meteor. Soc., P8.27, <https://ams.confex.com/ams/25SLS/webprogram/Paper175723.html>.
- Bunkers, M. J., and P. L. Smith, 2013: Comments on “An objective high-resolution hail climatology of the contiguous United States.” *Wea. Forecasting*, **28**, 915–917, <https://doi.org/10.1175/WAF-D-13-00020.1>.
- Cao, Q., Y. Hong, Y. Qi, Y. Wen, J. Zhang, J. J. Gourley, and L. Liao, 2013: Empirical conversion of the vertical profile of reflectivity from Ku-band to S-band frequency. *J. Geophys. Res. Atmos.*, **118**, 1814–1825, <https://doi.org/10.1002/jgrd.50138>.
- Carbone, R. E., J. W. Wilson, T. D. Keenan, and J. M. Hacker, 2000: Tropical island convection in the absence of significant topography. Part I: Life cycle of diurnally forced convection. *Mon. Wea. Rev.*, **128**, 3459–3480, [https://doi.org/10.1175/1520-0493\(2000\)128<3459:TICITA>2.0.CO;2](https://doi.org/10.1175/1520-0493(2000)128<3459:TICITA>2.0.CO;2).
- Carroll, R. J., and D. Ruppert, 1996: The use and misuse of orthogonal regression in linear errors-in variables models. *Amer. Stat.*, **50** (1), 1–6, <https://doi.org/10.2307/2685035>.
- Cecchini, M. A., A. J. Heymsfield, R. Honeyager, P. Field, L. A. T. Machado, and M. A. F. S. Dias, 2022: Revisiting the hail radar reflectivity–kinetic energy flux relation by combining T-matrix and discrete dipole approximation calculations to size distribution observations. *J. Atmos. Sci.*, **79**, 1927–1940, <https://doi.org/10.1175/JAS-D-20-0373.1>.
- Cecil, D. J., 2009: Passive microwave brightness temperatures as proxies for hailstorms. *J. Appl. Meteor. Climatol.*, **48**, 1281–1286, <https://doi.org/10.1175/2009JAMC2125.1>.
- , and C. B. Blankenship, 2012: Toward a global climatology of severe hailstorms as estimated by satellite passive microwave imagers. *J. Climate*, **25**, 687–703, <https://doi.org/10.1175/JCLI-D-11-00130.1>.

- Changnon, S. A., Jr., 1970: Hailstorms. *J. Atmos. Sci.*, **27**, 109–125, [https://doi.org/10.1175/1520-0469\(1970\)027<0109:H>2.0.CO;2](https://doi.org/10.1175/1520-0469(1970)027<0109:H>2.0.CO;2).
- Changnon, S. A., D. Changnon, and S. D. Hilberg, 2009: Hailstorms across the nation: An atlas about hail and its damages. Illinois State Water Survey Contract Rep. CR-2009-12, 101 pp., <https://www.isws.illinois.edu/pubdoc/cr/iswscr2009-12.pdf>.
- Cintineo, J. L., T. M. Smith, V. Lakshmanan, H. E. Brooks, and K. L. Ortega, 2012: An objective high-resolution hail climatology of the contiguous United States. *Wea. Forecasting*, **27**, 1235–1248, <https://doi.org/10.1175/WAF-D-11-00151.1>.
- Cotton, W. R., G. Bryan, and S. C. van den Heever, 2010: *Storm and Cloud Dynamics*. 2nd ed. Elsevier Science, 820 pp.
- Dahl, N. A., A. Shapiro, C. K. Potvin, A. Theisen, J. G. Gebauer, A. D. Schenkman, and M. Xue, 2019: High-resolution, rapid-scan dual-Doppler retrievals of vertical velocity in a simulated supercell. *J. Atmos. Oceanic Technol.*, **36**, 1477–1500, <https://doi.org/10.1175/JTECH-D-18-0211.1>.
- Dowdy, A. J., and Y. Kuleshov, 2014: Lightning climatology of Australia: Temporal and spatial variability. *Aust. Meteor. Oceanogr. J.*, **64**, 103–108, <https://doi.org/10.22499/2.6402.002>.
- , J. Soderholm, J. Brook, A. Brown, and H. McGowan, 2020: Quantifying hail and lightning risk factors using long-term observations around Australia. *J. Geophys. Res. Atmos.*, **125**, 2020JD033101, <https://doi.org/10.1029/2020JD033101>.
- Drosdowsky, W., and G. J. Holland, 1987: North Australian cloud lines. *Mon. Wea. Rev.*, **115**, 2645–2659, [https://doi.org/10.1175/1520-0493\(1987\)115<2645:NACL>2.0.CO;2](https://doi.org/10.1175/1520-0493(1987)115<2645:NACL>2.0.CO;2).
- Dworak, R., K. Bedka, J. Brunner, and W. Feltz, 2012: Comparison between GOES-12 overshooting-top detections, WSR-88D radar reflectivity, and severe storm reports. *Wea. Forecasting*, **27**, 684–699, <https://doi.org/10.1175/WAF-D-11-00070.1>.
- Eichner, J., 2019: Icy cricket balls from above. Accessed 7 April 2023, <https://www.munichre.com/topics-online/en/climate-change-and-natural-disasters/climate-change/Icy-cricket-balls-from-above.html>.
- Fabry, F., V. Meunier, B. P. Treserras, A. Cournoyer, and B. Nelson, 2017: On the climatological use of radar data mosaics: Possibilities and challenges. *Bull. Amer. Meteor. Soc.*, **98**, 2135–2148, <https://doi.org/10.1175/BAMS-D-15-00256.1>.
- Ferraro, R., J. Beauchamp, D. Cecil, and G. Heymsfield, 2015: A prototype hail detection algorithm and hail climatology developed with the Advanced Microwave Sounding Unit (AMSU). *Atmos. Res.*, **163**, 24–35, <https://doi.org/10.1016/j.atmosres.2014.08.010>.
- Foote, G. B., 1984: A study of hail growth utilizing observed storm conditions. *J. Climate Appl. Meteor.*, **23**, 84–101, [https://doi.org/10.1175/1520-0450\(1984\)023<0084:ASOHGU>2.0.CO;2](https://doi.org/10.1175/1520-0450(1984)023<0084:ASOHGU>2.0.CO;2).
- Frisby, E. M., and H. W. Sansom, 1967: Hail incidence in the tropics. *J. Appl. Meteor.*, **6**, 339–354, [https://doi.org/10.1175/1520-0450\(1967\)006<0339:HIITT>2.0.CO;2](https://doi.org/10.1175/1520-0450(1967)006<0339:HIITT>2.0.CO;2).
- Gabella, M., and R. Notarpietro, 2002: Ground clutter characterization and elimination in mountainous terrain. *Proc. ERAD*, Delft, The Netherlands, Copernicus, 305–311, <https://www.copernicus.org/erad/online/erad-305.pdf>.
- Goldstein, T., and S. Osher, 2009: The split Bregman method for L1-regularized problems. *SIAM J. Imaging Sci.*, **2**, 323–343, <https://doi.org/10.1137/080725891>.
- Gu, J.-Y., A. Ryzhkov, P. Zhang, P. Neiley, M. Knight, B. Wolf, and D.-I. Lee, 2011: Polarimetric attenuation correction in heavy rain at C band. *J. Appl. Meteor. Climatol.*, **50**, 39–58, <https://doi.org/10.1175/2010JAMC2258.1>.
- Gunturi, P., and M. K. Tippett, 2017: Managing severe thunderstorm risk: Impact of ENSO on US tornado and hail frequencies. Willis Re Inc., Tech. Rep., 5 pp.
- Hanstrum, B. N., K. J. Wilson, and S. L. Barrell, 1990a: Prefrontal troughs over southern Australia. Part I: A climatology. *Wea. Forecasting*, **5**, 22–31, [https://doi.org/10.1175/1520-0434\(1990\)005<0022:PTOSAP>2.0.CO;2](https://doi.org/10.1175/1520-0434(1990)005<0022:PTOSAP>2.0.CO;2).
- , —, and —, 1990b: Prefrontal troughs over southern Australia. Part II: A case study of frontogenesis. *Wea. Forecasting*, **5**, 32–46, [https://doi.org/10.1175/1520-0434\(1990\)005<0032:PTOSAP>2.0.CO;2](https://doi.org/10.1175/1520-0434(1990)005<0032:PTOSAP>2.0.CO;2).
- Heistermann, M., S. Jacobi, and T. Pfaff, 2013: Technical note: An open source library for processing weather radar data (wradlib). *Hydrol. Earth Syst. Sci.*, **17**, 863–871, <https://doi.org/10.5194/hess-17-863-2013>.
- Homeyer, C. R., and K. P. Bowman, 2017: Algorithm description document for version 3.1 of the three-dimensional gridded NEXRAD WSR-88D radar (GridRad) dataset. Tech. Rep., 23 pp., <https://gridrad.org/pdf/GridRad-v3.1-Algorithm-Description.pdf>.
- , J. D. McAuliffe, and K. M. Bedka, 2017: On the development of above-anvil cirrus plumes in extratropical convection. *J. Atmos. Sci.*, **74**, 1617–1633, <https://doi.org/10.1175/JAS-D-16-0269.1>.
- Hung, C.-W., and M. Yanai, 2004: Factors contributing to the onset of the Australian summer monsoon. *Quart. J. Roy. Meteor. Soc.*, **130**, 739–758, <https://doi.org/10.1256/qj.02.191>.
- Kaltenboeck, R., and A. Ryzhkov, 2013: Comparison of polarimetric signatures of hail at S and C bands for different hail sizes. *Atmos. Res.*, **123**, 323–336, <https://doi.org/10.1016/j.atmosres.2012.05.013>.
- Kumjian, M. R., K. Lombardo, and S. Loeffler, 2021: The evolution of hail production in simulated supercell storms. *J. Atmos. Sci.*, **78**, 3417–3440, <https://doi.org/10.1175/JAS-D-21-0034.1>.
- Kunz, M., and P. I. S. Kugel, 2015: Detection of hail signatures from single-polarization C-band radar reflectivity. *Atmos. Res.*, **153**, 565–577, <https://doi.org/10.1016/j.atmosres.2014.09.010>.
- Lakshmanan, V., T. Smith, K. Hondl, G. J. Stumpf, and A. Witt, 2006: A real-time, three-dimensional, rapidly updating, heterogeneous radar merger technique for reflectivity, velocity, and derived products. *Wea. Forecasting*, **21**, 802–823, <https://doi.org/10.1175/WAF942.1>.
- Langston, C., J. Zhang, and K. Howard, 2007: Four-dimensional dynamic radar mosaic. *J. Atmos. Oceanic Technol.*, **24**, 776–790, <https://doi.org/10.1175/JTECH2001.1>.
- Laroche, S., and I. Zawadzki, 1994: A variational analysis method for retrieval of three-dimensional wind field from single-Doppler radar data. *J. Atmos. Sci.*, **51**, 2664–2682, [https://doi.org/10.1175/1520-0469\(1994\)051<2664:AVAMFR>2.0.CO;2](https://doi.org/10.1175/1520-0469(1994)051<2664:AVAMFR>2.0.CO;2).
- Levizzani, V., and M. Setvák, 1996: Multispectral, high-resolution satellite observations of plumes on top of convective storms. *J. Atmos. Sci.*, **53**, 361–369, [https://doi.org/10.1175/1520-0469\(1996\)053<0361:MHSOO>2.0.CO;2](https://doi.org/10.1175/1520-0469(1996)053<0361:MHSOO>2.0.CO;2).
- Louf, V., and A. Protat, 2023: Real-time monitoring of weather radar network calibration and antenna pointing. *J. Atmos. Oceanic Technol.*, **40**, 823–844, <https://doi.org/10.1175/JTECH-D-22-0118.1>.
- Lukach, M., L. Foresti, O. Giot, and L. Delobbe, 2017: Estimating the occurrence and severity of hail based on 10 years of observations from weather radar in Belgium. *Meteor. Appl.*, **24**, 250–259, <https://doi.org/10.1002/met.1623>.
- May, P. T., A. R. Jameson, T. D. Keenan, P. E. Johnston, and C. Lucas, 2002: Combined wind profiler/polarimetric radar studies

- of the vertical motion and microphysical characteristics of tropical sea-breeze thunderstorms. *Mon. Wea. Rev.*, **130**, 2228–2239, [https://doi.org/10.1175/1520-0493\(2002\)130<2228:CWPPRS>2.0.CO;2](https://doi.org/10.1175/1520-0493(2002)130<2228:CWPPRS>2.0.CO;2).
- McAneney, J., B. Sandercock, R. Crompton, T. Mortlock, R. Mulsin, R. Pielke, and A. Gissing, 2019: Normalised insurance losses from Australian natural disasters: 1966–2017. *Environ. Hazards*, **18**, 414–433, <https://doi.org/10.1080/17477891.2019.1609406>.
- McMaster, H., 2001: Hailstorm risk assessment in rural New South Wales. *Nat. Hazards*, **24**, 187–196, <https://doi.org/10.1023/A:1011820206279>.
- Mroz, K., A. Battaglia, T. J. Lang, D. J. Cecil, S. Tanelli, and F. Tridon, 2017: Hail-detection algorithm for the GPM core observatory satellite sensors. *J. Appl. Meteor. Climatol.*, **56**, 1939–1957, <https://doi.org/10.1175/JAMC-D-16-0368.1>.
- Murillo, E. M., and C. R. Homeyer, 2019: Severe hail fall and hailstorm detection using remote sensing observations. *J. Appl. Meteor. Climatol.*, **58**, 947–970, <https://doi.org/10.1175/JAMC-D-18-0247.1>.
- , —, and J. T. Allen, 2021: A 23-year severe hail climatology using GridRad MESH observations. *Mon. Wea. Rev.*, **149**, 945–958, <https://doi.org/10.1175/MWR-D-20-0178.1>.
- Ni, X., C. Liu, D. J. Cecil, and Q. Zhang, 2017: On the detection of hail using satellite passive microwave radiometers and precipitation radar. *J. Appl. Meteor. Climatol.*, **56**, 2693–2709, <https://doi.org/10.1175/JAMC-D-17-0065.1>.
- Nisi, L., A. Hering, U. Germann, and O. Martius, 2018: A 15-year hail streak climatology for the alpine region. *Quart. J. Roy. Meteor. Soc.*, **144**, 1429–1449, <https://doi.org/10.1002/qj.3286>.
- Ortega, K. L., 2018: Evaluating multi-radar, multi-sensor products for surface hailfall diagnosis. *Electron. J. Severe Storms Meteor.*, **13** (1), <https://ejssm.org/archives/wp-content/uploads/2021/09/vol13-1.pdf>.
- , T. M. Smith, and G. J. Stumpf, 2006: Verification of multi-sensor, multi-radar hail diagnosis techniques. *Symp. on the Challenges of Severe Convective Storms*, Atlanta, GA, Amer. Meteor. Soc., P1.1, https://ams.confex.com/ams/Annual2006/techprogram/paper_104885.htm.
- Potts, R. J., T. D. Keenan, and P. T. May, 2000: Radar characteristics of storms in the Sydney area. *Mon. Wea. Rev.*, **128**, 3308–3319, [https://doi.org/10.1175/1520-0493\(2000\)128<3308:RCOSIT>2.0.CO;2](https://doi.org/10.1175/1520-0493(2000)128<3308:RCOSIT>2.0.CO;2).
- Prein, A. F., and G. J. Holland, 2018: Global estimates of damaging hail hazard. *Wea. Climate Extremes*, **22**, 10–23, <https://doi.org/10.1016/j.wace.2018.10.004>.
- Protat, A., D. Bouniol, E. J. O'Connor, H. Klein Baltink, J. Verlinde, and K. Widener, 2011: CloudSat as a global radar calibrator. *J. Atmos. Oceanic Technol.*, **28**, 445–452, <https://doi.org/10.1175/2010JTECHA1443.1>.
- , V. Louf, J. Soderholm, J. Brook, and W. Ponsonby, 2022: Three-way calibration checks using ground-based, ship-based, and spaceborne radars. *Atmos. Meas. Tech.*, **15**, 915–926, <https://doi.org/10.5194/amt-15-915-2022>.
- Pulkkinen, S., D. Nerini, A. A. Pérez Hortal, C. Velasco-Forero, A. Seed, U. Germann, and L. Foresti, 2019: Pysteps: An open-source python library for probabilistic precipitation nowcasting (v1.0). *Geosci. Model Dev.*, **12**, 4185–4219, <https://doi.org/10.5194/gmd-12-4185-2019>.
- Punge, H. J., K. M. Bedka, and M. Kunz, 2018: Continental scale hail frequency estimation from geostationary satellite detection. *Geophysical Research Abstracts*, Vol. 20, Abstract 15737, <https://meetingorganizer.copernicus.org/EGU2018/EGU2018-15737.pdf>.
- , —, —, S. D. Bang, and K. F. Itterly, 2021: Characteristics of hail hazard in South Africa based on satellite detection of convective storms. *Nat. Hazards Earth Syst. Sci.*, **23**, 1549–1576, <https://doi.org/10.5194/nhess-23-1549-2023>.
- Raupach, T. H., J. Soderholm, A. Protat, and S. C. Sherwood, 2023: An improved instability-shear hail proxy for Australia. *Mon. Wea. Rev.*, **151**, 545–567, <https://doi.org/10.1175/MWR-D-22-0127.1>.
- Ravasi, M., and I. Vasconcelos, 2020: Pylops—A linear-operator python library for scalable algebra and optimization. *SoftwareX*, **11**, 100361, <https://doi.org/10.1016/j.softx.2019.100361>.
- Riemann-Campe, K., K. Fraedrich, and F. Lunkeit, 2009: Global climatology of Convective Available Potential Energy (CAPE) and Convective Inhibition (CIN) in ERA-40 reanalysis. *Atmos. Res.*, **93**, 534–545, <https://doi.org/10.1016/j.atmosres.2008.09.037>.
- Rudin, L. I., S. Osher, and E. Fatemi, 1992: Nonlinear total variation based noise removal algorithms. *Physica D*, **60**, 259–268, [https://doi.org/10.1016/0167-2789\(92\)90242-F](https://doi.org/10.1016/0167-2789(92)90242-F).
- Ryzhkov, A. V., M. R. Kumjian, S. M. Ganson, and A. P. Khain, 2013: Polarimetric radar characteristics of melting hail. Part I: Theoretical simulations using spectral microphysical modeling. *J. Appl. Meteor. Climatol.*, **52**, 2849–2870, <https://doi.org/10.1175/JAMC-D-13-073.1>.
- Saltikoff, E., and Coauthors, 2019: An overview of using weather radar for climatological studies: Successes, challenges, and potential. *Bull. Amer. Meteor. Soc.*, **100**, 1739–1752, <https://doi.org/10.1175/BAMS-D-18-0166.1>.
- Schmetz, J., S. A. Tjemkes, M. Gube, and L. van de Berg, 1997: Monitoring deep convection and convective overshooting with METEOSAT. *Adv. Space Res.*, **19**, 433–441, [https://doi.org/10.1016/S0273-1177\(97\)00051-3](https://doi.org/10.1016/S0273-1177(97)00051-3).
- Schuster, S. S., R. J. Blong, and M. S. Speer, 2005: A hail climatology of the greater Sydney area and New South Wales, Australia. *Int. J. Climatol.*, **25**, 1633–1650, <https://doi.org/10.1002/joc.1199>.
- , —, and K. J. McAneney, 2006: Relationship between radar-derived hail kinetic energy and damage to insured buildings for severe hailstorms in eastern Australia. *Atmos. Res.*, **81**, 215–235, <https://doi.org/10.1016/j.atmosres.2005.12.003>.
- Shapiro, A., C. K. Potvin, and J. Gao, 2009: Use of a vertical vorticity equation in variational dual-Doppler wind analysis. *J. Atmos. Oceanic Technol.*, **26**, 2089–2106, <https://doi.org/10.1175/2009JTECHA1256.1>.
- , K. M. Willingham, and C. K. Potvin, 2010: Spatially variable advection correction of radar data. Part II: Test results. *J. Atmos. Sci.*, **67**, 3457–3470, <https://doi.org/10.1175/2010JAS3466.1>.
- Skripniková, K., and D. Rezáčová, 2014: Radar-based hail detection. *Atmos. Res.*, **144**, 175–185, <https://doi.org/10.1016/j.atmosres.2013.06.002>.
- Soderholm, J. S., H. McGowan, H. Richter, K. Walsh, T. M. Weckwerth, and M. Coleman, 2017a: An 18-year climatology of hailstorm trends and related drivers across southeast Queensland, Australia. *Quart. J. Roy. Meteor. Soc.*, **143**, 1123–1135, <https://doi.org/10.1002/qj.2995>.
- , H. A. McGowan, H. Richter, K. Walsh, T. Wedd, and T. M. Weckwerth, 2017b: Diurnal preconditioning of subtropical coastal convective storm environments. *Mon. Wea. Rev.*, **145**, 3839–3859, <https://doi.org/10.1175/MWR-D-16-0330.1>.

- , K. I. Turner, J. P. Brook, T. Wedd, and J. Callaghan, 2019: High-impact thunderstorms of the Brisbane metropolitan area. *J. South. Hemisphere Earth Syst. Sci.*, **69**, 239–251, <https://doi.org/10.1071/ES19017>.
- , V. Louf, J. Brook, and A. Protat, 2022: Australian operational weather radar level 1b dataset. National Computing Infrastructure, accessed 8 August 2023, <https://www.openradar.io/operational-network>.
- Stržinar, G., and G. Skok, 2018: Comparison and optimization of radar-based hail detection algorithms in Slovenia. *Atmos. Res.*, **203**, 275–285, <https://doi.org/10.1016/j.atmosres.2018.01.005>.
- Stumpf, G. J., T. M. Smith, and J. Hocker, 2004: New hail diagnostic parameters derived by integrating multiple radars and multiple sensors. *22nd Conf. on Severe Local Storms*, Hyannis, MA, Amer. Meteor. Soc. P7.8, https://ams.confex.com/ams/11aram22sls/techprogram/paper_81451.htm.
- Sturman, A. P., and N. J. Tapper, 1996: *The Weather and Climate of Australia and New Zealand*. Oxford University Press, 476 pp.
- Taszarek, M., J. T. Allen, T. Púčik, K. A. Hoogewind, and H. E. Brooks, 2020: Severe convective storms across Europe and the United States. Part II: ERA5 environments associated with lightning, large hail, severe wind, and tornadoes. *J. Climate*, **33**, 10263–10286, <https://doi.org/10.1175/JCLI-D-20-0346.1>.
- Tippett, M. K., J. T. Allen, V. A. Gensini, and H. E. Brooks, 2015: Climate and hazardous convective weather. *Curr. Climate Change Rep.*, **1**, 60–73, <https://doi.org/10.1007/s40641-015-0006-6>.
- Troupin, C., and Coauthor, 2012: Generation of analysis and consistent error fields using the Data Interpolating Variational Analysis (DIVA). *Ocean Modell.*, **52–53**, 90–101, <https://doi.org/10.1016/j.ocemod.2012.05.002>.
- Waldvogel, A., W. Schmid, and B. Federer, 1978: The kinetic energy of hailfalls. Part I: Hailstone spectra. *J. Appl. Meteor.*, **17**, 515–520, [https://doi.org/10.1175/1520-0450\(1978\)017<0515:TKEOHP>2.0.CO;2](https://doi.org/10.1175/1520-0450(1978)017<0515:TKEOHP>2.0.CO;2).
- Walsh, K., and Coauthors, 2016: Natural hazards in Australia: Storms, wind and hail. *Climatic Change*, **139**, 55–67, <https://doi.org/10.1007/s10584-016-1737-7>.
- Wapler, K., and T. P. Lane, 2012: A case of offshore convective initiation by interacting land breezes near Darwin, Australia. *Meteor. Atmos. Phys.*, **115**, 123–137, <https://doi.org/10.1007/s00703-011-0180-6>.
- Warren, R. A., A. Protat, S. T. Siems, H. A. Ramsay, V. Louf, M. J. Manton, and T. A. Kane, 2018: Calibrating ground-based radars against TRMM and GPM. *J. Atmos. Oceanic Technol.*, **35**, 323–346, <https://doi.org/10.1175/JTECH-D-17-0128.1>.
- , H. A. Ramsay, S. T. Siems, M. J. Manton, J. R. Peter, A. Protat, and A. Pillalamarri, 2020: Radar-based climatology of damaging hailstorms in Brisbane and Sydney, Australia. *Quart. J. Roy. Meteor. Soc.*, **146**, 505–530, <https://doi.org/10.1002/qj.3693>.
- Wendt, N. A., and I. L. Jirak, 2021: An hourly climatology of operational MRMS MESH-diagnosed severe and significant hail with comparisons to storm data hail reports. *Wea. Forecasting*, **36**, 645–659, <https://doi.org/10.1175/WAF-D-20-0158.1>.
- Wilson, C. J., K. L. Ortega, and V. Lakshmanan, 2009: Evaluating multi-radar, multi-sensor hail diagnosis with high resolution hail reports. *25th Conf. on Int. Interactive Information and Processing Systems (IIPS) for Meteorology, Oceanography, and Hydrology*, Phoenix, AZ, Amer. Meteor. Soc., P2.9, https://ams.confex.com/ams/89annual/techprogram/paper_146206.htm.
- Witt, A., M. D. Eilts, G. J. Stumpf, J. T. Johnson, E. D. W. Mitchell, and K. W. Thomas, 1998: An enhanced hail detection algorithm for the WSR-88D. *Wea. Forecasting*, **13**, 286–303, [https://doi.org/10.1175/1520-0434\(1998\)013<0286:AEHDAF>2.0.CO;2](https://doi.org/10.1175/1520-0434(1998)013<0286:AEHDAF>2.0.CO;2).
- York, D., 1966: Least-squares fitting of a straight line. *Can. J. Phys.*, **44**, 1079–1086, <https://doi.org/10.1139/p66-090>.
- Zhou, Z., Q. Zhang, J. T. Allen, X. Ni, and C.-P. Ng, 2021: How many types of severe hailstorm environments are there globally? *Geophys. Res. Lett.*, **48**, e2021GL095485, <https://doi.org/10.1029/2021GL095485>.